

Seeing Double with K2: Testing Re-inflation with Two Remarkably Similar Planets around Red Giant Branch Stars

Samuel K. Grunblatt¹, Daniel Huber^{1,2,3,4}, Eric Gaidos⁵, Eric D. Lopez⁶, Andrew W. Howard^{1,7}, Howard T. Isaacson⁸, Evan Sinukoff^{1,7}, Andrew Vanderburg^{9,10,17}, Larissa Nofi^{1,11}, Jie Yu², Thomas S. H. North^{4,12}, William Chaplin^{4,12}, Daniel Foreman-Mackey^{13,16,18}, Erik Petigura^{7,19}, Megan Ansdell⁸, Lauren Weiss^{14,20}, Benjamin Fulton^{1,7,21}, and Douglas N. C. Lin¹⁵ ¹ Institute for Astronomy, University of Hawaii, 2680 Woodlawn Drive, Honolulu, HI 96822, USA; skg@ifa.hawaii.edu Sydney Institute for Astronomy (SIfA), School of Physics, University of Sydney, NSW 2006, Australia ³ SETI Institute, 189 Bernardo Avenue, Mountain View, CA 94043, USA ⁴ Stellar Astrophysics Centre, Department of Physics and Astronomy, Aarhus University, Ny Munkegade 120, DK-8000 Aarhus C, Denmark Department of Geology & Geophysics, University of Hawaii at Manoa, Honolulu, Hawaii 96822, USA NASA Goddard Space Flight Center, Greenbelt, MD 20771, USA California Institute of Technology, Pasadena, CA 91125, USA ⁸ Department of Astronomy, University of California Berkeley, Berkeley, CA 94720, USA Harvard-Smithsonian Center for Astrophysics, 60 Garden St., Cambridge, MA 02138, USA Department of Astronomy, The University of Texas at Austin, Austin, TX 78712, USA Lowell Observatory, 1400 W. Mars Hill Road, Flagstaff, AZ 86001, USA ¹² School of Physics and Astronomy, University of Birmingham, Birmingham, B15 2TT, UK ¹³ Astronomy Department, University of Washington, Box 351580, Seattle, WA 98195, USA ¹⁴ Institut de Recherche sur les Exoplanètes, Université de Montréal, Montréal, QC, Canada UCO/Lick Observatory, Board of Studies in Astronomy and Astrophysics, University of California, Santa Cruz, California 95064, USA Center for Computational Astrophysics, Flatiron Institute, 162 Fifth Avenue, New York, NY 10010, USA Received 2017 June 19; revised 2017 September 15; accepted 2017 October 10; published 2017 November 27

Abstract

Despite more than 20 years since the discovery of the first gas giant planet with an anomalously large radius, the mechanism for planet inflation remains unknown. Here, we report the discovery of K2-132b, an inflated gas giant planet found with the NASA K2 Mission, and a revised mass for another inflated planet, K2-97b. These planets orbit on ≈ 9 day orbits around host stars that recently evolved into red giants. We constrain the irradiation history of these planets using models constrained by asteroseismology and Keck/High Resolution Echelle Spectrometer spectroscopy and radial velocity measurements. We measure planet radii of $1.31 \pm 0.11 R_J$ and $1.30 \pm 0.07 R_J$, respectively. These radii are typical for planets receiving the current irradiation, but not the former, zero age main-sequence irradiation of these planets. This suggests that the current sizes of these planets are directly correlated to their current irradiation. Our precise constraints of the masses and radii of the stars and planets in these systems allow us to constrain the planetary heating efficiency of both systems as $0.03\%_{-0.02\%}^{+0.03\%}$. These results are consistent with a planet re-inflation scenario, but suggest that the efficiency of planet re-inflation may be lower than previously theorized. Finally, we discuss the agreement within 10% of the stellar masses and radii, and the planet masses, radii, and orbital periods of both systems, and speculate that this may be due to selection bias in searching for planets around evolved stars.

Key words: planet–star interactions – planets and satellites: detection – planets and satellites: gaseous planets – planets and satellites: physical evolution – stars: fundamental parameters – stars: oscillations

1. Introduction

Since the first measurement of planet radii outside our solar system (Charbonneau et al. 2000; Henry et al. 2000), it has been known that gas giant planets with equilibrium temperatures greater than 1000 K tend to have radii larger than model predictions (Burrows et al. 1997; Bodenheimer et al. 2001; Guillot & Showman 2002). Moreover, a correlation has been observed between incident stellar radiation and planetary radius inflation (Burrows et al. 2000; Laughlin et al. 2011; Lopez & Fortney 2016). The diversity of mechanisms proposed to explain the inflation of giant planets (Baraffe et al. 2014) can be split into two general classes: mechanisms where stellar irradiation is deposited directly into the planet's deep interior,

driving adiabatic heating of the planet and thus inflating its radius (Class I; e.g., Bodenheimer et al. 2001; Batygin & Stevenson 2010; Ginzburg & Sari 2016), and mechanisms where no energy is deposited into the deep planetary interior and the inflationary mechanism simply acts to slow the radiative cooling of the planet's atmosphere, preventing it from losing its initial heat and thus radius inflation from its formation (Class II; e.g., Burrows et al. 2000; Chabrier & Baraffe 2007; Wu & Lithwick 2013). These mechanism classes can be distinguished by measuring the radii of planets that have recently experienced large changes in irradiation, such as planets orbiting red giant stars at 10-30 day orbital periods (Lopez & Fortney 2016). To quantify the distinction between mechanism classes, we require that planets (1) approach or empirical planet inflation threshold of $2 \times 10^8 \, \mathrm{erg \ s^{-1} \ cm^{-2}}$ ($\approx 150 \, F_{\oplus}$ Demory & Seager 2011) after reaching the zero age main sequence, and (2) experience a change in incident flux large enough that the planet radius would increase significantly, assuming it followed the trend

¹⁷ NSF Graduate Research Fellow.

¹⁸ Sagan Fellow.

¹⁹ Hubble Fellow.

²⁰ Trottier Fellow.

²¹ Texaco Fellow.

between incident flux and planet radius found by Laughlin et al. (2011). If such planets are currently inflated, heat from irradiation must have been deposited directly into the planet interior, indicating that Class I mechanisms must be at play, whereas if these planets are not inflated, no energy has been transferred from the planet surface into its deep interior, and thus Class II mechanisms are favored. By constraining the efficiency of heat transfer to inflated planets orbiting evolved host stars, we can distinguish the efficiency of these two classes of inflation mechanisms (Ginzburg & Sari 2016; Lopez & Fortney 2016).

To constrain the properties of giant planet inflation, we search for transiting giant planets orbiting low-luminosity red giant branch (LLRGB) stars with the NASA K2 Mission (Howell et al. 2014; Huber 2016). These stars are large enough that we can detect their oscillations to perform asteroseismology, but small enough that gas giant planet transits are still detectable in K2 long-cadence data. Close-in planets in these systems have experienced significant changes in irradiation over time. The first planet discovered by our survey, K2-97b, was published by Grunblatt et al. (2016, hereafter referred to as G16). Using a combination of asteroseismology, transit analysis, and radial velocity measurements, G16 measured the mass and radius of this planet to be $1.10 \pm 0.12 M_{\rm J}$ and $1.31 \pm 0.11 R_{\rm J}$, respectively. This implied a direct heating efficiency of 0.1%–0.5%, suggesting that the planet radius was directly influenced by the increase in irradiation caused by the host-star evolution.

Here, we present additional radial velocity data that revise the mass of K2-97 to $0.48 \pm 0.07\,M_{\rm J}$, as well as the discovery of the second planet in our survey, K2-132b, with a radius of $1.30 \pm 0.07\,R_{\rm J}$ and mass of $0.49 \pm 0.06\,M_{\rm J}$. These planets currently receive incident fluxes between 700 and $1100\,F_{\oplus}$, but previously received fluxes between 100 and $350\,F_{\oplus}$ when the host stars were on the main sequence. Quantifying the incident flux evolution of these systems allows us to estimate the planetary heating efficiency and distinguish between planetary inflation mechanisms.

2. Observations

2.1. K2 Photometry

In the K2 extension to the NASA Kepler mission, multiple fields along the ecliptic are observed almost continuously for approximately 80 days (Howell et al. 2014). EPIC 211351816 (now known as K2-97; G16) was selected for observation as part of the K2 Guest Observer Proposal GO5089 (PI: Huber) and observed in Campaign 5 of K2 during the first half of 2015. EPIC 228754001 (now known as K2-132) was selected and observed in Campaign 10 of K2 as part of the K2 Guest Observer Proposal GO10036 (PI: Huber) in the second half of 2016. As the Kepler telescope now has unstable pointing due to the failure of two of its reaction wheels, it is necessary to correct for the pointing-dependent error in the flux received per pixel. We produced a light curve by simultaneously fitting thruster systematics, low-frequency variability, and planet transits with a Levenberg-Marquardt minimization algorithm, using a modified version of the pipeline from Vanderburg et al. (2016). These light curves were then normalized and smoothed with a 75 hr median filter, and points deviating from the mean by more than 5σ were removed. By performing a box leastsquares transit search for transits with 5-40 day orbital periods

and 3–30 hr transit durations on these light curves using the algorithm of Kovács et al. (2002), we identified transits of \approx 500 and \approx 1000 ppm, respectively. Using the techniques of G16 and those described in Section 4.1, we determined that the transits came from an object that was planetary in nature. Figure 1 shows our adopted light curves for K2-97 and K2-132.

2.2. Imaging with Keck/NIRC2 AO

To check for potential blended background stars, we obtained natural guide-star adaptive optics (AO) images of K2-132 through the broad K' filter ($\lambda_{\rm center}=2.124~\mu{\rm m}$) with the Near-Infrared Camera (NIRC2) at the Keck II telescope on Maunakea during the night of UT 2017 January 25. The narrow camera (pixel scale 0.011) was used for all sets of observations. No additional sources were detected within \sim 3011 of the star. The contrast ratio of the detection limit is more than 7 magnitudes at 0.0111 of the star. These data were collected to quantify the possibility of potential false positive scenarios in these systems, and the relevant analysis is described in Section 4.2. Previous analysis by G16 of NIRC2 AO images of K2-97 reached effectively identical conclusions.

Images were processed using a custom Python pipeline that linearized, dark-subtracted, flattened, sky-subtracted, and coadded the images (Metchev & Hillenbrand 2009). A cutout \sim 3."0 across, centered on the star, was made and inserted back into the processed image as a simulated companion. A contrast curve was generated by decreasing the brightness and angular separation of the simulated companion with respect to the primary, until the limits of detection (3.0σ) were reached. Figure 2 plots the contrast ratio for detection as a function of distance from the source K2-132.

2.3. High-resolution Spectroscopy and Radial Velocity Measurements with the Keck/High Resolution Echelle Spectrometer (HIRES)

We obtained a high-resolution, high signal-to-noise spectrum of K2-97 and K2-132 using HIRES on the 10 meter Keck I telescope at Maunakea Observatory on the Big Island of Hawaii. HIRES provides a spectral resolution of roughly 65,000 in the wavelength range of 4500–6200 Å (Vogt et al. 1994) and has been used to both characterize over 1000 *Kepler* planet host stars (Petigura et al. 2017) as well as confirm and provide precise parameters of over 2000 *Kepler* planets (Fulton et al. 2017; Johnson et al. 2017). Our spectra were analyzed using the software package SpecMatch (Petigura 2015) following the procedure outlined in G16.

Radial velocity (RV) measurements were obtained between 2016 January 27 and 2017 April 10 using HIRES on the Keck I Telescope at the Maunakea Observatory in Hawaii. Individual measurements are listed in Table 1 and shown in Figure 9. All RV spectra were obtained through an iodine gas cell. We collected three measurements of K2-97 with Keck/HIRES in 2016, and seven additional measurements in 2017. All 11 measurements of K2-132 were taken between 2016 December and 2017 April. Fits to the RV data were made using the publicly available software package RadVel (Fulton & Petigura 2017) and confirmed through independent analysis, presented in Section 4.2. We adopted the same method for RV analysis as described in G16 (Butler et al. 1996).

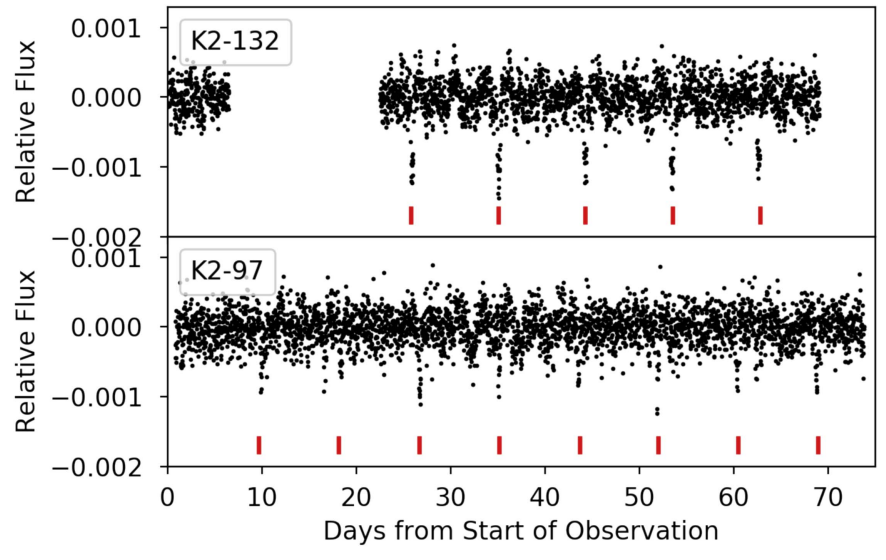


Figure 1. Detrended *K2* light curves of K2-97 (bottom) and K2-132 (top). These light curves were produced using a modified method of the pipeline presented in Vanderburg et al. (2016), where both instrument systematics and planet transit were modeled simultaneously to prevent transit dilution. The light curve has been normalized and median-filtered as well as unity subtracted. Individual transits are visible by eye and are denoted by red fiducial marks.

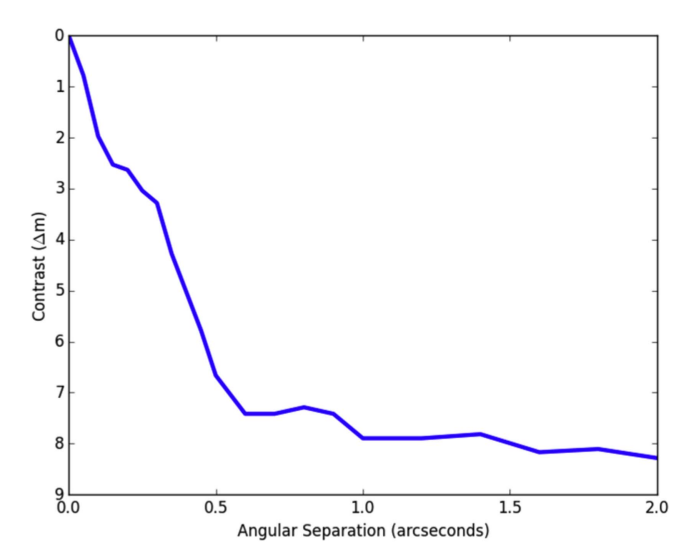


Figure 2. Contrast in differential K' magnitude as a function of angular separation from K2-132. No companions were detected within 3'' of the source. G16 found effectively identical results for K2-97.

3. Host Star Characteristics

3.1. Spectroscopic Analysis

In order to obtain precise values for the effective temperature and metallicity of the star, we used the software package SpecMatch (Petigura 2015) and adopted the spectroscopic analysis method described in G16 for both stars. SpecMatch searches a grid of synthetic model spectra from Coelho et al. (2005) to find the best-fit values for the $T_{\rm eff}$, $\log g$, [Fe/H], mass, and radius of the star. We report the effective temperature $T_{\rm eff}$ and metallicity [Fe/H] from the SpecMatch analysis here. We also note that the $\log g_{\rm spec} = 3.19 \pm 0.07$ value from the spectroscopic analysis is fully consistent with the asteroseismic determination of $\log g_{\rm AS} = 3.26 \pm 0.008$ (see the next section for details), so no iteration was needed to recalculate $T_{\rm eff}$ and metallicity once the asteroseismic parameters had been determined.

Table 1
Radial Velocities

Star	BJD-2440000	RV (m s ⁻¹)	Prec. (m s ⁻¹)
K2-97	17414.927751	-4.91	1.79
K2-97	17422.855362	-38.94	1.72
K2-97	17439.964043	-17.95	2.22
K2-97	17774.905553	-44.03	1.85
K2-97	17790.840786	-50.74	1.77
K2-97	17802.819367	7.96	1.76
K2-97	17803.836621	38.90	1.64
K2-97	17830.802784	32.84	1.77
K2-97	17853.790069	23.05	1.78
K2-97	17854.774479	46.68	1.85
K2-132	17748.099507	-30.32	1.95
K2-132	17764.115738	25.80	1.66
K2-132	17766.139232	-40.85	1.96
K2-132	17776.065142	-26.91	1.54
K2-132	17789.093812	26.09	1.74
K2-132	17790.091515	45.40	1.68
K2-132	17791.071462	46.31	1.85
K2-132	17794.992775	-22.43	1.88
K2-132	17803.927316	-37.99	1.91
K2-132	17830.066681	-34.92	1.83
K2-132	17854.937650	50.42	1.78

Note. The precisions listed here are instrumental only and do not take into account the uncertainty introduced by stellar jitter. For moderately evolved stars like K2-97 and K2-132, RV jitter on relevant timescales can reach $\gtrsim 10~\text{m s}^{-1}$ (see G16 and Section 4.2 for more details).

3.2. Asteroseismology

Stellar oscillations are stochastically excited and damped at characteristic frequencies due to turbulence from convection in the outer layers of the star. The characteristic oscillation timescales or frequencies are determined by the internal structure of the star. By measuring the peak frequency of the power excess ($\nu_{\rm max}$) and frequency spacing between individual radial orders of oscillation ($\Delta \nu$), the stellar mass, radius, and density can all be determined to 10% precision or better.

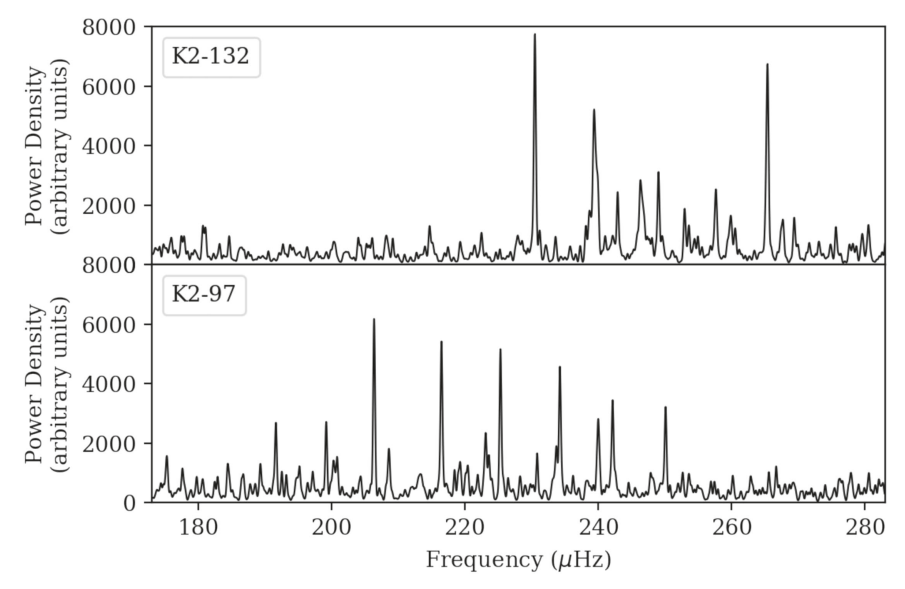


Figure 3. Power density of K2-132 (top) and K2-97 (bottom) estimated from K2 light curves, centered on the frequency range where stellar oscillations can be detected for low-luminosity red giant branch stars. In both cases, stellar oscillations are clearly visible. Note that the power excess of K2-132 does not display a typical Gaussian solar-like oscillation profile due to its proximity to the K2 long-cadence Nyquist frequency (283 μHz).

Similar to G16, we employed asteroseismology using K2 long-cadence data by measuring stellar oscillation frequencies to determine precise fundamental properties of the evolved host star K2-132. Figure 3 compares the power spectra of K2-97 and K2-132. Compared to the power excess of K2-97 near \approx 220 μ Hz (75 minutes), K2-132 oscillates with higher frequencies near \approx 250 μ Hz (65 minutes), indicative of a smaller, less evolved RGB star.

Figure 3 also shows that the power excess of K2-132 is less broad and triangular than K2-97. This is most likely due to the proximity of the power excess to the long-cadence Nyquist frequency (283.24 μ Hz), causing an attenuation of the oscillation amplitude due to aliasing effects. The proximity to the Nyquist frequency also implies that the real power excess could lie either below or above the Nyquist frequency (Chaplin et al. 2014; Yu et al. 2016). To discern between these scenarios, we applied the method of Yu et al. (2016) to distinguish the real power excess from its aliased counterpart. Based on the power-law relation determined by Yu et al. (2016), $\Delta \nu =$ $0.262 \times 0.770 \nu_{\text{max}}$, as well as a consistent measurement of $\Delta \nu = 18.46 \pm 0.26 \,\mu\text{Hz}$ both above and below the Nyquist frequency, we find $\nu_{\rm max} = 245.65 \pm 3.51 \,\mu{\rm Hz}$, suggesting the true oscillations lie below the Nyquist frequency. To validate this conclusion, we also constructed the global oscillation pattern via the ε - $\Delta \nu$ relation (Stello et al. 2016) for the given $\Delta \nu$ value and found that the power excess below the Nyquist frequency demonstrates the expected frequency phase shift ε and matches the expected frequency pattern more precisely. The collapsed échelle diagram generated from the Huber et al. (2009) pipeline indicates that the total power of the l=2modes is smaller than that for the l = 0 modes, which also suggests that the real power excess is below the Nyquist frequency (Yu et al. 2016). Independent asteroseismic analyses using both a separate pipeline for asteroseismic value estimation as well as using light curves detrended using different methods recovered asteroseismic parameters in good agreement with the values shown here (North et al. 2017). In addition, the asteroseismic analyses of G16 also strongly agree with our results for K2-97.

To estimate stellar properties from ν_{max} and $\Delta\nu$, we use the asteroseismic scaling relations of Brown et al. (1991) and Kjeldsen & Bedding (1995):

$$\frac{\Delta\nu}{\Delta\nu_{\odot}} \approx f_{\Delta\nu} \left(\frac{\rho}{\rho_{\odot}}\right)^{0.5},\tag{1}$$

$$\frac{\nu_{\rm max}}{\nu_{\rm max,\odot}} \approx \frac{g}{g_{\odot}} \left(\frac{T_{\rm eff}}{T_{\rm eff,\odot}}\right)^{-0.5}.$$
 (2)

Equations (1) and (2) can be rearranged to solve for mass and radius:

$$\frac{M}{M_{\odot}} \approx \left(\frac{\nu_{\text{max}}}{\nu_{\text{max},\odot}}\right)^{3} \left(\frac{\Delta\nu}{f_{\Delta\nu}\Delta\nu_{\odot}}\right)^{-4} \left(\frac{T_{\text{eff}}}{T_{\text{eff},\odot}}\right)^{1.5} \tag{3}$$

$$\frac{R}{R_{\odot}} \approx \left(\frac{\nu_{\text{max}}}{\nu_{\text{max},\odot}}\right) \left(\frac{\Delta \nu}{f_{\Delta \nu}} \Delta \nu_{\odot}\right)^{-2} \left(\frac{T_{\text{eff}}}{T_{\text{eff},\odot}}\right)^{0.5}.$$
 (4)

Our adopted solar reference values are $\nu_{\rm max,\odot}=3090~\mu{\rm Hz}$ and $\Delta\nu_\odot=135.1~\mu{\rm Hz}$ (Huber et al. 2011a), as well as $T_{\rm eff,\odot}=5777~{\rm K}$.

It has been shown that asteroseismically determined masses are systematically offset from masses determined using other methods, particularly for the most evolved stars (Sharma et al. 2016). To address this, we also adopt a correction factor of $f_{\Delta\nu}=0.994$ for K2-97 from G16 and calculate a correction factor $f_{\Delta\nu}=0.998$ for K2-132 following the procedure of Sharma et al. (2016). Our final adopted values for the stellar radius, mass, $\log g$, and densities of K2-97 and K2-132 are calculated using these modified asteroseismic scaling relations and are listed in Table 2.

4. Light-curve Analysis and Planetary Parameters

4.1. Gaussian Process Transit Models

The transits of K2-97b and K2-132b were first identified using the box least-squares procedure described in G16 and Section 2.1 (Kovács et al. 2002). The detrended light curves,

 Table 2

 Stellar and Planetary Properties for K2-97 and K2-132

Property	K2-97	K2-132	Source
Kepler Magnitude	12.41	11.65	Huber et al. (2016)
Temperature, $T_{\rm eff}$	$4790\pm90~\mathrm{K}$	$4840\pm90~\mathrm{K}$	spectroscopy
Metallicity [Fe/H]	$+0.42\pm0.08$	-0.01 ± 0.08	spectroscopy
Stellar Mass, $M_{\rm star}$	$1.16 \pm 0.12 M_{\odot}$	$1.08 \pm 0.08 M_{\odot}$	asteroseismology
Stellar Radius, R _{star}	$4.20\pm0.14R_{\odot}$	$3.85 \pm 0.13 R_{\odot}$	asteroseismology
Density, ρ_*	$0.0222 \pm 0.0004 \mathrm{g cm^{-3}}$	$0.0264 \pm 0.0008 \mathrm{g \ cm}^{-3}$	asteroseismology
$\log g$	3.26 ± 0.01	3.297 ± 0.007	asteroseismology
Age	$7.6_{-2.3}^{+5.5} \text{ Gyr}$	$8.5^{+4.5}_{-2.8} \mathrm{Gyr}$	isochrones
Planet Radius, R_p	$1.31 \pm 0.11 R_{\rm J}$	$1.30 \pm 0.07 R_{ m I}$	GP+transit model
Orbital Period, Porb	8.4061 ± 0.0015 days	9.1751 ± 0.0025 days	GP+transit model
Planet Mass, M_p	$0.48\pm0.07M_{\rm J}$	$0.49\pm0.06M_{\rm J}$	RV model

Note. All values for the K2-97 system are taken from G16, with the exception of the system age, which was recalculated for this publication. See Section 5.1 for a discussion of the system age calculations.

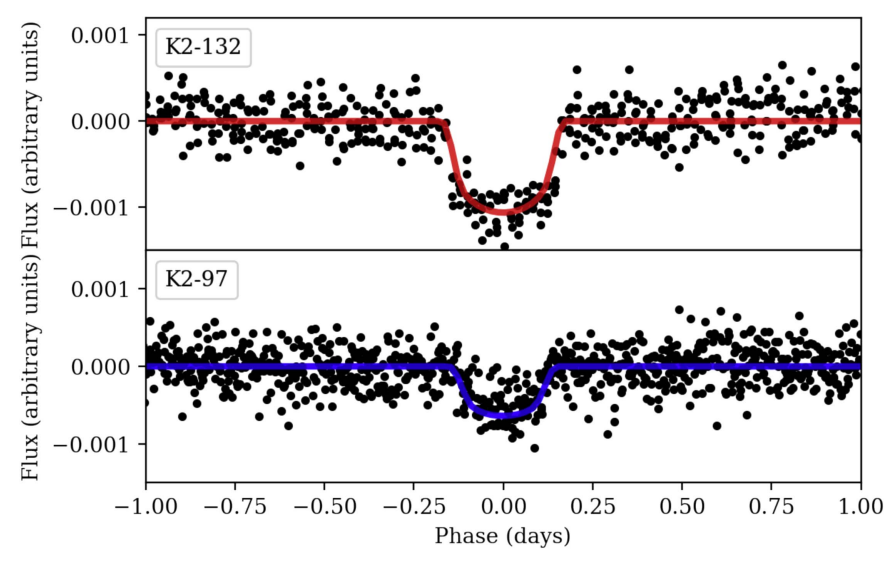


Figure 4. Detrended *K2* light curves of K2-132 (top) and K2-97 (bottom), folded at the observed transit period. Preliminary transit fit parameters were established through a box least-squares search (Kovács et al. 2002); our final pure transit models (Mandel & Agol 2002) are shown by solid lines.

phase-folded at the period detected by the box least-squares search and fit with best-fit transit models, are shown in Figure 4.

Evolved stars display correlated stellar variation on timescales of hours to weeks due to stellar granulation and oscillation (Mathur et al. 2012), leading to systematic errors in transit parameter estimation (Carter & Winn 2009; Barclay et al. 2015). Thus, a stochastically driven and damped simple harmonic oscillator can be used to both describe the stellar oscillation and granulation noise in a light curve as well as characterize the fundamental physical properties of the star.

In G16, we used a squared exponential Gaussian process estimation model to remove stellar variability in the K2 light curve and measure the transit depth of K2-97b precisely. Here, we used a Gaussian process estimation kernel that assumes stellar variability can be described by a stochastically driven damped simple harmonic oscillator, modified from the method of G16. We also present results using the previously tested squared exponential Gaussian process kernel, which has been successfully applied to remove correlated noise in various one-dimensional data sets in the past (Gibson et al. 2012; Dawson

et al. 2014; Haywood et al. 2014; Barclay et al. 2015; Grunblatt et al. 2015, 2016).

We describe the covariance of the time-series data as an $N \times N$ matrix Σ , where

$$\Sigma_{ij} = \sigma_i^2 \delta_{ij} + k(\tau_{ij}), \tag{5}$$

where σ_i is the observational uncertainty, δ_{ij} is the Kronecker delta, and $k(\tau_{ij})$ is the so-called covariance kernel function that quantifies the correlations between times t_i and t_j (Rasmussen & Williams 2006).

Following Foreman-Mackey et al. (2017), the kernel function we use can be expressed as

$$k(\tau_{ij}) = \sum_{n=1}^{N} [a_n \exp(-c_n \tau_{ij}) \cos(d_n \tau_{ij}) + b_n \exp(-c_n \tau_{ij}) \cos(d_n \tau_{ij})],$$
(6)

where a_n , b_n , c_n , and d_n are a set of constants that define the *n*th term in our kernel function. We then redefine these constants a_n , b_n , c_n , and d_n as the simple harmonic oscillator components

 Q_n , $\omega_{0,n}$, and $S_{0,n}$, such that

$$k(\tau_{ij}) = S_0 \omega_0 Q e^{-\frac{\omega_0 \tau_{ij}}{2Q}}$$

$$\times \begin{cases} \cosh(\eta \omega_0 \tau_{ij}) + \frac{1}{2\eta Q} \sinh(\eta \omega_0 \tau_{ij}), \\ 0 < Q < 1/2 \\ 2(1 + \omega_0 \tau_{ij}), \\ Q = 1/2 \\ \cos(\eta \omega_0 \tau_{ij}) + \frac{1}{2\eta Q} \sin(\eta \omega_0 \tau_{ij}), \\ 1/2 < Q, \end{cases}$$

$$(7)$$

where Q_n represents the quality factor or damping coefficient of the nth simple harmonic oscillator, $\omega_{0,n}$ represents the resonant frequency of the nth simple harmonic oscillator, $S_{0,n}$ is proportional to the power at $\omega = \omega_{0,n}$, and $\eta = \sqrt{1 - (4Q^2)^{-1}}$. We find that we can describe the stellar variability seen in our data as a sum of three simple harmonic oscillator components, similar to many asteroseismic models used to describe stellar oscillations (e.g., Huber et al. 2009). This allows us to create a physically motivated model of stellar variability from which we can produce rigorous probabilistic measurements of asteroseismic quantities using only time domain information.

Our simple harmonic oscillator Gaussian process model consists of three main components: two $Q = 1/\sqrt{2}$ terms, which are commonly used to model granulation in asteroseismic analyses (Harvey 1985; Huber et al. 2009; Kallinger et al. 2014), and one $Q \gg 1$ term, which has been shown to describe stellar oscillations effectively (Foreman-Mackey et al. 2017), to describe the envelope of the stellar oscillation signal. The resonant frequency ω_0 of this component is thus an independent estimate of ν_{max} , and we compare our asteroseismic $\nu_{\rm max}$ measurement made from the analysis in the frequency domain to the $\nu_{\rm max}$ we generate here through a pure time domain analysis. We find a good agreement between our independent estimates of $\nu_{\rm max}$ for K2-132 using both traditional asteroseismic analysis methods ($\nu_{\rm max} = 245.65 \pm 3.51 \,\mu{\rm Hz}$) and our simple harmonic oscillator Gaussian process model estimate ($\nu_{\text{max,GP}} = 241.8 \pm 1.9 \,\mu\text{Hz}$).

Following the procedure of G16, we incorporate a transit model with the initial parameters determined by the box least-squares analysis as the mean function from which residuals and the Gaussian process kernel parameters are estimated. By exploring the probability space through a Monte Carlo Markov Chain (MCMC) routine where a likelihood for the combined transit and variability model is calculated repeatedly, we simultaneously optimize both the stellar variability and transit parameters. The logarithm of the posterior likelihood of our model is given by

$$\log[\mathcal{L}(\mathbf{r})] = -\frac{1}{2}\mathbf{r}^{\mathrm{T}}\mathbf{\Sigma}^{-1}\mathbf{r} - \frac{1}{2}\log|\mathbf{\Sigma}| - \frac{n}{2}\log(2\pi), \quad (8)$$

where r is the vector of the residuals of the data after removal of the mean function (in our case, r is the light curve signal minus the transit model) and n is the number of data points.

We repeat this process using both the new simple harmonic oscillator Gaussian process estimator as well as the squared exponential Gaussian process estimator. We illustrate our

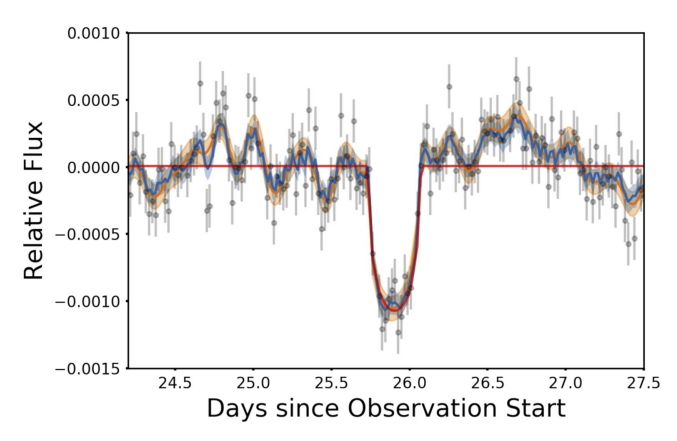


Figure 5. Illustration of a transit in the K2-132 light curve. The best-fit transit model is shown in red. A combined best-fit transit + squared exponential Gaussian process (SE GP) model is shown in orange, with 1σ model uncertainties shown by the orange shaded region. A combined best-fit transit + simple harmonic oscillator Gaussian process (SHO GP) model is shown with the 1σ uncertainties in blue. In addition to having smaller uncertainties than the SE GP model, the SHO GP model also captures variations on different timescales more accurately and is physically motivated by the oscillation signal of the star.

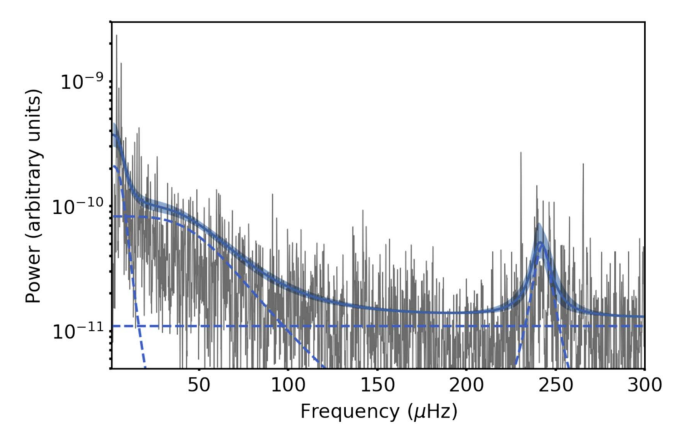


Figure 6. Power spectrum of the K2-132 light curve (gray) overlaid with the simple harmonic oscillator Gaussian process model (solid blue line). Uncertainties in the model are given by the blue contours. The individual component terms of the Gaussian process model are shown by the dotted lines. The two low-Q components account for the granulation noise signal at low frequencies. The high-Q component traces the envelope of the stellar oscillation signal and allows us to estimate the frequency of the maximum power of the stellar oscillations, and thus determine $\nu_{\rm max}$ from the time domain

transit + GP models and uncertainties in the time domain in Figure 5 and our simple harmonic oscillator GP model in the frequency domain in Figure 6. We find that our simple harmonic oscillator Gaussian process estimation is able to capture variation on a wider range of timescales than the squared exponential Gaussian process estimation, and also features smaller uncertainty distributions in the time domain. In addition, the simple harmonic oscillator model exploits the tridiagonal structure of a covariance matrix generated by a mixture of exponentials such that it scales linearly, rather than cubically, with the size of the input data set. This means the squared exponential Gaussian process estimation takes over an order of magnitude more time to generate for the entire light curve than the simple harmonic oscillator model despite having less than half the number of parameters. Furthermore, the squared exponential estimate provides a poor estimate of the

Table 3
Posterior Probabilities from Light Curve and Radial Velocity MCMC
Modeling of K2-132

Parameter	Posterior Value	Prior
$\rho(\text{g cm}^{-3})$	$0.0264^{+0.0008}_{-0.0007}$	N(0.0264; 0.0008)
T ₀ (BJD-2454833)	$2757.1491^{+0.008}_{-0.009}$	U(5.5; 9.5)
P _{orb} (days)	$9.1751^{+0.0023}_{-0.0027}$	U(9.0; 9.4)
b	$0.848^{+0.007}_{-0.008}$	$U(0.0, 1.0 + R_p/R_*)$
R_p/R_*	$0.0325^{+0.0014}_{-0.0011}$	U(0.0, 0.5)
$\nu_{\rm max,GP}~(\mu{\rm Hz})$	$241.8^{+1.9}_{-1.9}$	U(120, 280)
$K (m s^{-1})$	$42.1_{-4.2}^{+4.3}$	U(0, 100)
$T_{0,RV}$ (BKJD % P_{orb})	$3.57^{+0.19}_{-0.19}$	$\mathcal{U}(0.0, P_{\mathrm{orb}})$
$\sigma_{\rm RV}~({\rm m~s}^{-1})$	$11.5^{+4.1}_{-2.6}$	U(0, 100)

Note. \mathcal{N} indicates a normal distribution with mean and standard deviation given respectively. \mathcal{U} indicates a uniform distribution between the two given boundaries. Ephemerides were fit relative to the first measurement in the sample and then later converted to the Barycentric *Kepler* Julian Date (BKJD).

appearance of the data in the frequency domain, whereas the simple harmonic oscillator estimate is able to reproduce both an estimate of the granulation background as well as the stellar oscillation signal, two of the strongest features of the stellar signal in the frequency domain. The similarity between the simple harmonic oscillator estimate and the power spectral density estimate from the light curve is particularly remarkable considering all fitting was done using time domain information, suggesting that this simple harmonic oscillator estimation technique may be a valuable prototype for designing a technique to perform ensemble asteroseismology using only time domain information (Brewer & Stello 2009; Foreman-Mackey et al. 2017).

Due to the benefits from employing the simple harmonic oscillator Gaussian process estimation technique to extract the planet-to-star radius ratio, we choose to use the results from this model as our accepted values for calculating planet radius. We show the best-fit results for selected parameters of interest in Table 3. The posterior distributions of the planet radius estimated with both methods are shown in Figure 7, illustrating that planet radius estimates by both Gaussian process techniques are in very good agreement.

Figure 8 illustrates the parameter distributions for the full transit+GP model. All parameters are sampled in logarithmic space. The first nine parameters are the simple harmonic oscillator component terms of the model, as well as the white noise σ . The last four parameters of the model are the transit parameters R_p/R_* , stellar density ρ , phase parameter T_0 , and impact parameter b,. Correlations between b and R_p/R_* can be seen. Uniform box priors were placed on all GP parameters to ensure physical values. In addition, $\ln \omega_{0,0}$ has a strict lower bound of 1.1 as the data quality at frequencies lower than 3 μ Hz is too poor to warrant modeling. $\ln Q_2$ has a strict upper bound of 4.2 to ensure that the envelope of stellar oscillations is modeled as opposed to individual frequencies of stellar oscillation (which correspond to higher Q values), and $\omega_{0.2}$ has bounds of 200 and 280 μ Hz to ensure that the excess modeled corresponds to the asteroseismic excess determined previously. The lower bound of the white noise parameter $\ln \sigma$ posterior distribution is also set by a uniform box prior, as the median absolute deviation of the light curve (162 ppm, not a variable in our model) is sufficient to capture the uncorrelated variability in our data, and thus any additional white noise

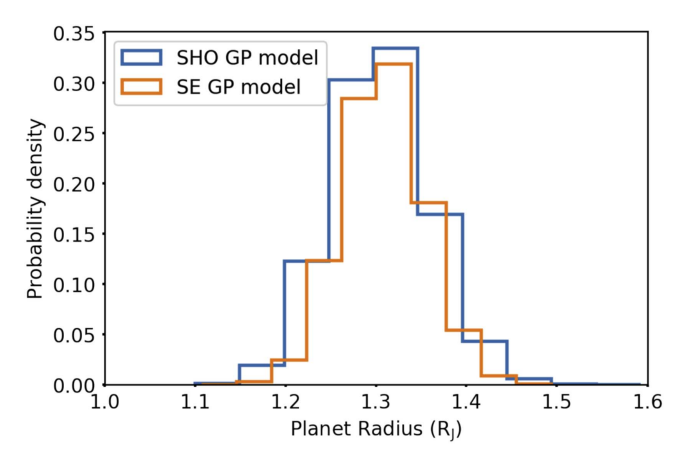


Figure 7. Posterior distributions of the planet radius based on our stellar parameters derived from asteroseismology and transit depth measured in our transit + squared exponential Gaussian process model (SE GP model, orange) and our transit + simple harmonic oscillator Gaussian process model (SHO GP model, blue) for K2-132b. Parameters differ between the two models, but both provide estimates of R_p/R_* which can be converted into planet radius and directly compared. We find that our squared exponential (SE) GP model strongly agrees with our simple harmonic oscillator (SHO) GP model.

below this level is equally likely given this data set. A Gaussian prior has been placed on ρ according to its asteroseismic determination in Section 3.2. The eccentricity is fixed to zero for our transit model, based on arguments explained in Section 5.3.

In addition, the quadratic limb-darkening parameters γ_1 and γ_2 in our transit model were fixed to the (Claret & Bloemen 2011) stellar atmosphere model grid values of 0.6505 and 0.1041, respectively. These values correspond to the stellar model atmosphere closest to the measured temperature, surface gravity, and metallicity of the host star. As Barclay et al. (2015) demonstrate that limb-darkening parameters are poorly constrained by the transits of a giant planet orbiting a giant star with four years of *Kepler* photometry, our much smaller sample of transits, all of which are polluted by stellar variability, would not be sufficient to constrain limb darkening.

In order to evaluate parameter convergence, the Gelman–Rubin statistic was calculated for each parameter distribution and forced to reach 1.01 or smaller (Gelman & Rubin 1992). In order to achieve this, 30 MCMCs with 50,000 steps each were used to produce parameter distributions.

4.2. Radial Velocity Analysis, Planetary Confirmation, and False Positive Assessment

We modeled the Keck/HIRES RV measurements of K2-97 and K2-132 following the method of G16, with slight modifications. Similarly to G16, we produced an initial fit for the systems using the publicly available Python package RadVel (Fulton & Petigura 2017), and then fit the data independently as a Keplerian system with amplitude K, phase ϕ , white noise σ , RV zeropoint z, and a period θ predetermined and fixed from the transit analysis.

We assume that the eccentricity of the planet is fixed to zero in our transit and RV analysis based on dynamical arguments presented in Section 5.3. Nevertheless, the data are not sufficient to precisely constrain the eccentricity of this system. Jones et al. (2017) explore the possibilities of eccentricity in this system in more detail.

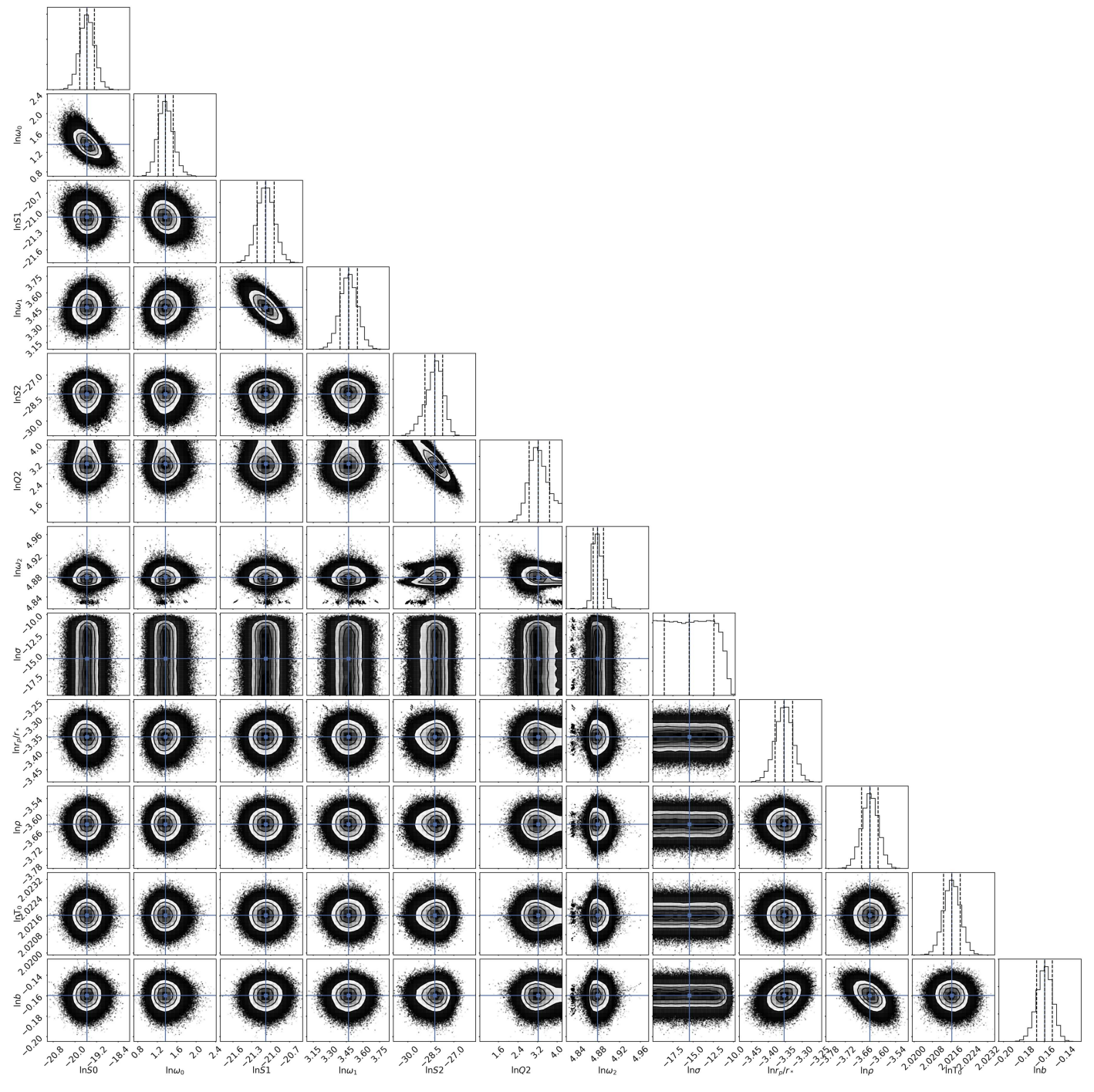


Figure 8. Posterior distributions for the complete transit + GP model of K2-132. The first eight parameters are part of the GP model, whereas the last four are components of the transit model. Individual parameter posterior distributions are shown along the diagonal, while correlations between two parameters are shown by the off-diagonal, two-dimensional distributions. Median values are indicated by the blue lines; the dotted lines indicate 1σ uncertainties. Priors are discussed in further detail within the text.

Due to the relatively high degree of scatter within our RV measurements and the known increase in RV scatter due to stellar jitter as stars evolve up the red giant branch (Huber et al. 2011b), we fit for the astrophysical white noise error and add it to our RV measurement errors in quadrature, finding typical errors of 10–15 m s⁻¹. Non-transiting planets orbiting at different orbital periods may also add additional uncertainty to our measurements. We probed modestly for these planets by collecting RV measurements spanning multiple orbital periods of the transiting planet in both systems, confirming that the

dominant periodic RV signal coincides with the transit events. Median values and uncertainties on Keplerian model parameters were determined using MCMC analysis powered by emcee (Foreman-Mackey et al. 2013). We illustrate the RV measurements of both systems as well as the best-fit Keplerian models in Figure 9.

Figure 10 illustrates the posterior distributions for the RV model amplitude K, phase ϕ , zeropoint z, and uncorrelated uncertainty σ . In order to evaluate parameter convergence, the Gelman–Rubin statistic was calculated for each parameter

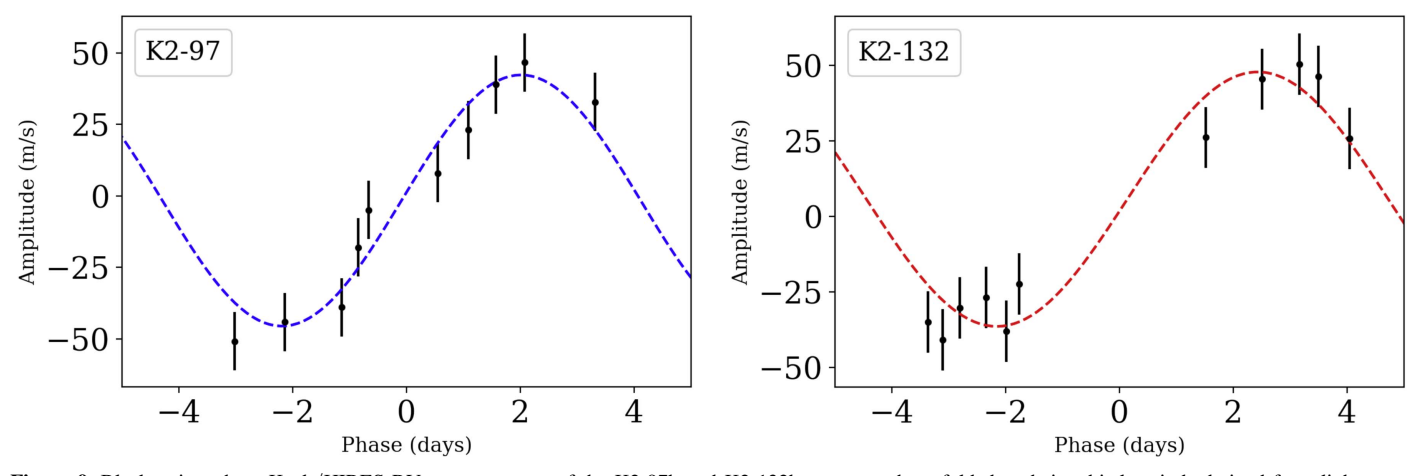


Figure 9. Black points show Keck/HIRES RV measurements of the K2-97b and K2-132b systems, phase-folded at their orbital periods derived from light-curve analysis. Errors correspond to the measurement errors of the instrument added in quadrature to the measured astrophysical jitter. The dashed colored curves correspond to the one-planet Keplerian orbit fit to the data using the median value of the posterior distribution for each fitted Keplerian orbital parameter. Parameter posterior distributions were determined through MCMC analysis with emcee.

distribution and forced to reach 1.01 or smaller (Gelman & Rubin 1992). In order to achieve this, 30 MCMCs with 50,000 steps each were used to produce parameter distributions.

The initial confirmation of the K2-97b system included the three earliest Keck/HIRES measurements shown here as well as the RVs measured by the Automated Planet Finder (APF) Levy Spectrometer at the Lick Observatory in California. Due to the relatively large uncertainties on the APF measurements, the earlier mass estimates were dominated by the Keck/HIRES data. However, the small number of Keck/HIRES measurements spanned less than 10% of the entire orbit. This limited coverage, as well as an overly conservative estimate of stellar jitter, resulted in an overestimate of the mass of K2-97b in G16. The additional coverage by Keck/HIRES since the publication of G16 has negated the issues brought by the relatively large uncertainties of the APF measurements and effectively expanded the RV phase coverage to >50%. This revealed that the previous characterization of stellar jitter was an underestimate and the planet mass was significantly lower than estimated in G16.

We quantitatively evaluated false positive scenarios for K2-132b as in G16 and more thoroughly described in Gaidos et al. (2016) using our adaptive optics (AO) imaging and lack of a long-term trend in our RV measurements of K2-132 to rule out background eclipsing binaries or a hierarchical triple (companion eclipsing binary). We reject these scenarios because the nearly 8 hr transit duration is much too long compared to that expected for an eclipsing binary with the same period, provided that the system is not highly eccentric (e > 0.3), and our RV measurements rule out a scenario involving two stellar-mass objects. Preliminary evidence from our RV data also suggests that an eccentricity of e > 0.3 is unlikely for this system, but a full exploration of eccentricity scenarios is beyond the scope of this article (see Section 5.3 for more details). Furthermore, a background evolved star that was unresolved by our AO imaging is too unlikely, $\ll 2 \times 10^{-7}$, and the dilution by the foreground (target) star too high to explain the signal. Evolved companions are ruled out by our AO imaging to within 0"2 and stellar counterparts within \sim 1 au are ruled out by the absence of an RV drift.

We cannot rule out companions that could cause a small systematic error in planet radius due to dilution of the transit signal. However, to change the planet radius by one standard error, the minimum contrast ratio in the *Kepler* bandpass must be 0.1. If the star is cooler than K2-132 (likely, since a hotter, more massive star would be more evolved), then the contrast in the *K*-band of our NIRC2 imaging would be even higher. We can rule out all such stars exterior to 0.15 arcsec (~50 au) of the primary; the absence of a significant drift in the Doppler data or a second set of lines in the HIRES spectrum rules out stellar companions within about 1 au. Regardless, transit dilution by an unresolved companion would mean that the planet is actually *larger* than what we estimate and inflation even more likely.

5. Constraining Planet Inflation Scenarios

5.1. Irradiation Histories of K2-97b and K2-132b

Planets with orbital periods of <30 days will experience levels of irradiation comparable to that of typical hot Jupiters for more than 100 Myr during post-main-sequence evolution. Thus, we can test planet inflation mechanisms by examining how planets respond to increasing irradiation as the host star leaves the main sequence. Following the nomenclature of Lopez & Fortney (2016), if the inflation mechanism requires direct heating and thus falls into Class I, the planet's radius should increase around a post-main-sequence star. However, if the inflation mechanism falls into Class II, requiring delayed cooling, there should be no effect on planet radius as a star enters the red giant phase and re-inflation will not occur. As K2-97b and K2-132b are inflated now but may not have received irradiation significantly above the inflation threshold on the main sequence, they provide valuable tests for the reinflation hypothesis. Furthermore, these systems can be used to constrain the mechanisms of heat transfer and dissipation within planets (e.g., Tremblin et al. 2017).

To trace the incident flux history of both planets, we used a grid of Parsec v2.1 evolutionary tracks (Bressan et al. 2012) with metallicities ranging from [Fe/H] = -0.18 to 0.6 dex and masses ranging from 0.8 to $1.8 M_{\odot}$. Compared to G16, we used an improved MC sampling scheme by interpolating evolutionary tracks to a given mass and metallicity following normal

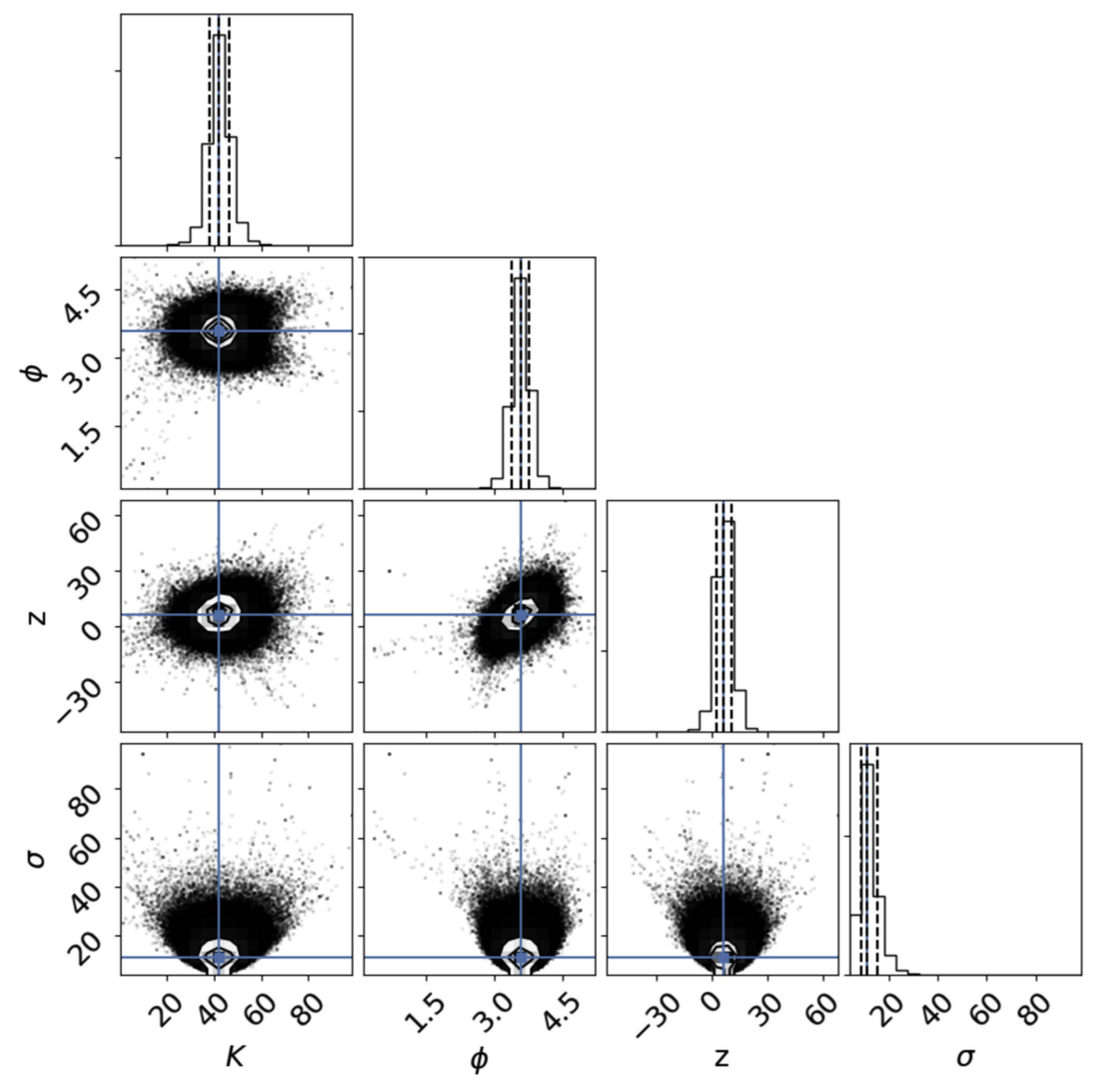


Figure 10. Posterior distributions for the complete RV model of K2-132b. Individual parameter posterior distributions are shown along the diagonal, while correlations between two parameters are shown by the off-diagonal, two-dimensional distributions. Median values are indicated by the blue lines; dotted lines indicate 1σ uncertainties.

distributions with the values given in Table 2, and tracing the incident flux across equal evolutionary states as indicated by the "phase" parameter in Parsec models. We performed 1000 iterations for each system, and the resulting probability distributions are shown as a function of evolutionary state in Figure 11. We note that each evolutionary state corresponds to a different age depending on the stellar mass and metallicity. Representative ages for the best-fit stellar parameters of K2-132 are given on the upper x-axis. Current incident flux and age ranges for the planets were determined by restricting models to within 1σ of the measured temperature and radius of each system (Table 2).

Figure 11 demonstrates that both planets lie near the Demory & Seager (2011) empirical threshold for inflated planets at the

zero age main sequence. Planets below this threshold have typical planet radii below $1.0\,R_{\rm J}$. Just after the end of their main-sequence lifetimes, the irradiance on these planets reached the median incident flux on a typical $1.2\,R_{\rm J}$ planet determined by the median incident flux values for confirmed planets listed in the NASA Exoplanet Archive with radii consistent with $1.2\,R_{\rm J}$. As the maximum radius of H/He planets determined by structural evolutionary models has been found to be $1.2\,R_{\rm J}$, we treat this as the maximum size at which planets could be considered "uninflated," providing an incident flux boundary range for inflation more conservative than the lower limit established by the Demory & Seager (2011) or the Laughlin et al. (2011) planetary effective temperature–radius

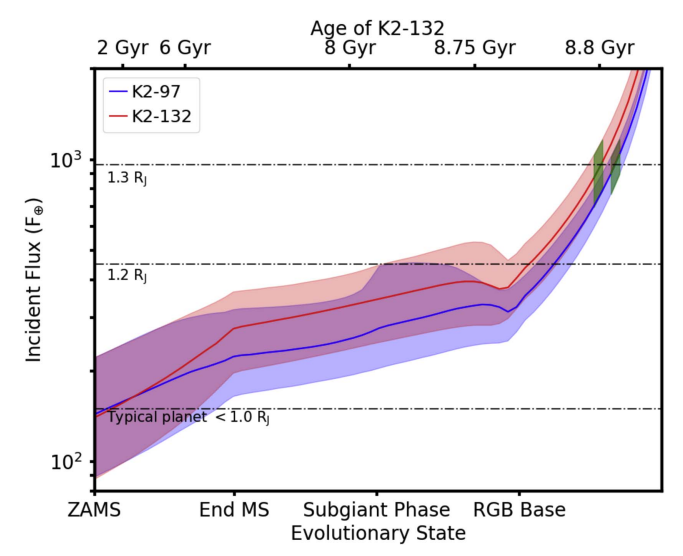


Figure 11. Incident flux as a function of evolutionary state for K2-97b and K2-132b. The current incident flux on the planets is denoted in green. The solid blue and red lines and shaded areas show the median and 1σ confidence interval considering uncertainties in stellar mass and metallicity. The black dashed lines correspond to the median incident fluxes for known populations of hot gas giant planets of different radii (Demory & Seager 2011, NASA Exoplanet Archive, 2017 September 14). The top axis shows representative ages for the best-fit stellar parameters of K2-132.

anomaly models. Now that the host stars have evolved off the main sequence, these planets have reached incident flux values typical for $1.3\,R_{\rm J}$ planets. The median incident flux for $1.3\,R_{\rm J}$ planets was determined from a sample of confirmed planets taken from the NASA Exoplanet Archive (accessed 2017 September 14).

The average main-sequence fluxes of K2-97b and K2-132b are 170^{+140}_{-60} F_{\oplus} and 190^{+150}_{-80} F_{\oplus} , respectively. These values are more than 4.5σ from the median fluxes of well-characterized $1.3\,R_{\rm J}$ planets. However, the current incident fluxes of $900\pm200\,F_{\oplus}$ on these planets, shown in green in Figure 11, is strongly consistent with the observed incident flux range of $1.3\,R_{\rm J}$ planets, suggesting that the radii of these planets are tied closely to their current irradiation. Despite the fact that the planets crossed the empirical threshold for inflation relatively early on in their lifetimes, if at all, the planets did not receive sufficient flux to display significant radius anomalies or be inflated to their observed sizes until post-main-sequence evolution.

Though the current incident fluxes of the planets in this study lie much closer to the median value for $1.3\,R_{\rm J}$ planets, it is important to note that their incident flux is also consistent with the $1.2\,R_{\rm J}$ planet population, as the standard deviation in both planet populations is $\gtrsim 500\,F_{\oplus}$. This is to be expected, as the vast majority of confirmed planet radii are not measured to within 10% or less, and thus the $1.2\,R_{\rm J}$ and $1.3\,R_{\rm J}$ planet populations are not distinct.

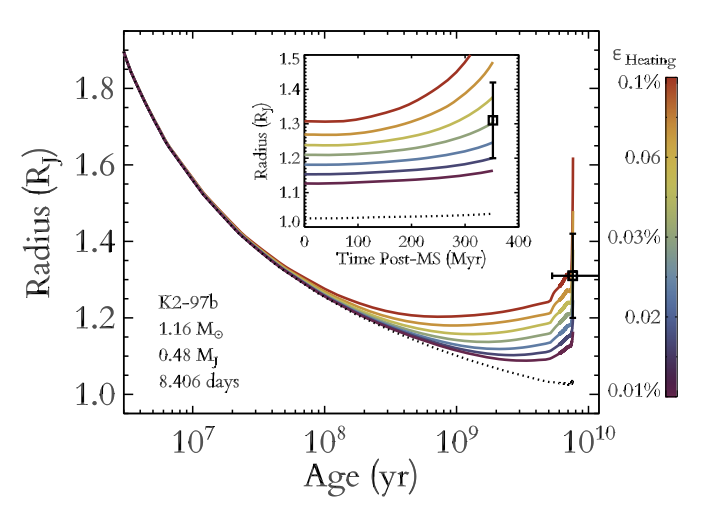
5.2. Comparing Re-inflation and Delayed Cooling Models

Figure 12 illustrates the Class I models for the radius evolution of K2-97b and K2-132b, assuming the best-fit values for planet mass, radius, and orbital period. Each of these models assumes a constant planetary heating efficiency, defined to be the fraction of energy a planet receives from its host star that is deposited into the planetary interior, causing adiabatic heating and inflation of the planet. The colors of the

various planetary evolution curves correspond to different planetary heating efficiencies ranging from 0.01% to 0.1%, assuming a planet with the best-fit planet mass at a constant orbital distance from a star with the best-fit stellar mass calculated here. The incident flux on the planet is then calculated as a function of time using the MESA stellar evolutionary tracks (Choi 2016). From this, the planet radius is calculated by convolving the Kelvin-Helmholtz cooling time with planetary heating at a consistent efficiency with respect to the incident stellar flux over the lifetime of the system. The black dotted lines correspond to planetary evolution with no external heat source. Post-main-sequence evolution is shown with higher time resolution in the insets. Based on the calculated planet radii, we estimate a heating efficiency of $0.03\%^{+0.04\%}_{-0.02\%}$ for K2-97b and $0.03\%^{+0.03\%}_{-0.01\%}$ for K2-132b. Uncertainties on the heating efficiency were calculated by running additional models for each system with both masses and radii lowered/raised by one standard deviation. As planet mass and radius uncertainties are not perfectly correlated, using such a method to calculate planetary heating efficiency should provide conservative errors.

Based on these two particular planets, the heating efficiency of gas giant planets via the post-main-sequence evolution of their host stars is strongly consistent between both planets but smaller than theories predict (Lopez & Fortney 2016), and disagrees with the previous estimate of planetary heating efficiency of 0.1%-0.5% made by G16. This disagreement stems from the overestimate of the mass of K2-97b in the previous study. As the radii of lower density planets are more sensitive to heating and cooling effects than those of higher density, the required heating to inflate a 1.1 $M_{\rm J}$ planet to 1.3 $R_{\rm J}$ is significantly larger than the heating necessary to inflate a $0.5 M_{\rm I}$ planet to the same size. These new estimates of planet heating efficiency tentatively suggest that if planetary re-inflation occurred in these systems, the process is not as efficient as previous studies suggested (Lopez & Fortney 2016).

Slowed planetary cooling cannot be entirely ruled out as the cause for large planet radii, as the planets are not larger than they would have been during their pre-main-sequence formation. Figure 13 illustrates the various delayed cooling tracks that could potentially produce these planets. Different colored curves correspond to cooling models where the Kelvin-Helmholtz cooling time is increased by a constant factor. K2-97b and K2-132b are shown in bold, whereas planets with masses of 0.4–0.6 $M_{\rm J}$, incident fluxes of 100–300 F_{\oplus} , and host stars smaller than $2R_{\odot}$ (to ensure that they have not begun RGB evolution) are shown in gray (specifically, these planets are K2-30b, Kepler-422b, OGLE-TR-111b, WASP-11b, WASP-34b, and WASP-42b). It can be seen that the mainsequence planets have systematically smaller radii and thus suggest delayed cooling rates that are significantly different from those which would be inferred from the planets in this study. The required cooling delay factor for the post-mainsequence planets studied here is 20-250, significantly more than the factor of $\sim 1-10$ for main-sequence cases. Delayed cooling models predict a decrease in planet radius with age, which strongly disagrees with the data shown here. Re-inflation models predict the opposite. Thus, we conclude that Class I re-inflation mechanisms are more statistically relevant than Class II mechanisms in the evolution of K2-97b and K2-132b,



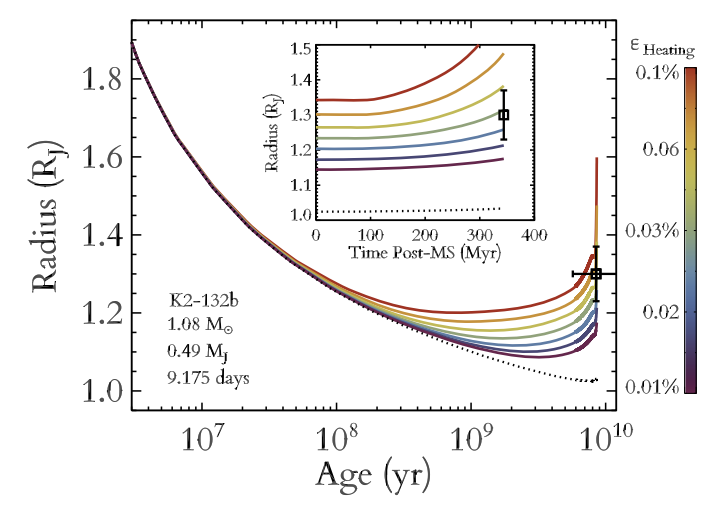


Figure 12. Planetary radius as a function of time for K2-97b (left) and K2-132b (right), shown for different values of heating efficiency. We assume the best-fit values for the stellar mass and the planetary mass and radius, and a planetary composition of a H/He envelope surrounding a $10 M_{\oplus}$ core of heavier elements. The dotted line corresponds to a scenario with no planetary heating. The inset shows the post-main-sequence evolution at a finer time resolution. The measured planet radii are consistent with heating efficiencies of $0.03\%_{-0.02\%}^{+0.04\%}$ and $0.03\%_{-0.1\%}^{+0.04\%}$, respectively.

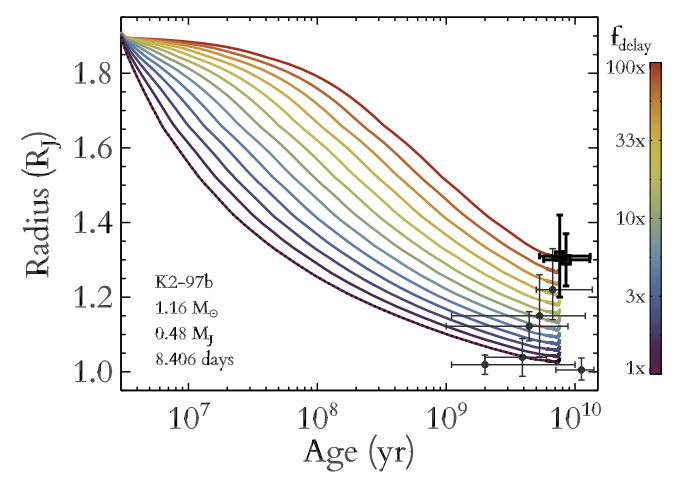


Figure 13. Planetary radius as a function of time for K2-97b and K2-132b (bold), as well other similar mass planets with similar main-sequence fluxes orbiting main-sequence stars. Colored tracks represent scenarios where planets begin at an initial radius of $1.85\,R_{\rm J}$ and then contract according to the Kelvin–Helmholtz timescale delayed by the factor given by the color of the track. All main-sequence planets seem to lie on tracks that would favor different delayed cooling factors than the post-main-sequence planets studied here.

and hence stellar irradiation is likely to be the direct cause of warm and hot Jupiter inflation.

Furthermore, the assumption of a $10\,M_\oplus$ core is low compared to the inferred core masses of cooler non-inflated giants. Using the planet–core-mass relationship of Thorngren et al. (2016), we predict core masses of $\approx 37\,M_\oplus$ for both K2-97b and K2-132b. These higher core masses would significantly increase the required heating efficiencies to $0.10\%_{-0.05\%}^{+0.09\%}$ for K2-97b and $0.14\%_{-0.04\%}^{+0.07\%}$ for K2-132b, or delayed cooling factors of 300– $3000\times$ for these planets. Though these values suggest better agreement with previous results (e.g., G16), we report the conservative outcomes assuming $10\,M_\oplus$ cores to place a lower limit on the efficiency of planetary heating.

5.3. Eccentricity Effects

Jones et al. (2017) independently report a non-zero eccentricity for K2-132b based on the HIRES data presented

here and additional RV measurements obtained with other instruments. Since transit parameters are often degenerate, an inaccurate eccentricity could result in an inaccurate planet radius (e.g., Eastman et al. 2013) and thus potentially affect our conclusions regarding planet re-inflation.

A non-circular orbit would be surprising given the expected tidal circularization timescale for such planets. Our estimated planet parameters suggest a timescale of $\tau_e\sim 6$ Gyr using the relation of Gu et al. (2003) and assuming a tidal quality factor $Q_p\approx 10^6$, comparable to Jupiter (Ogilvie & Lin 2004; Wu 2005). This suggests that the orbit of this planet should have been circularized before post-main-sequence evolution, as long as no other companion could have dynamically excited the system. However, these timescale estimates are very sensitive to planet density and tidal quality factor, and adjusting these parameters within errors can result in estimates of $\tau_e<1$ Gyr as well as $\tau_e>10$ Gyr. Thus, we cannot rule out a non-zero eccentricity for this system based on tidal circularization timescale arguments alone.

We also used the relations of Bodenheimer et al. (2001) to determine the tidal circularization energy and thus the tidal radius inflation that would be expected for this system. We find that the tidal inflation should be negligible for this system even for potentially high eccentricity. Thus, if this planet were to be on an eccentric orbit, we should still be able to distinguish between tidal and irradiative planet inflation.

We attempted to model the eccentricity of this system and obtained results that were consistent with our circular model. However, these tests resulted in non-convergent posterior chains, and thus we cannot rule out a non-negligible eccentricity for this system. Additional RV measurements should help to constrain the eccentricity of this system, and clarify if and how eccentricity affects the planet radius presented here.

5.4. Selection Effects and the Similarity of Planet Parameters

K2-97 and K2-132 are remarkably similar: the stellar radii and masses and planet radii, masses, and orbital periods agree within 10%. This begs the question: is it only coincidence that these systems are so similar, is it the product of convergent

planetary evolution, or is it the result of survey bias or selection effect? Here, we investigate the last possibility.

Two effects modulate the intrinsic distribution of planets as a function of mass M, radius R, and orbital period P to produce the observed occurrence in a survey of evolved stars: the detection of the planet by transit and the lifetime of planets against orbital decay due to tides raised on large, low-density host stars. A deficit of giant planets close to evolved stars (Kunitomo et al. 2011) as well as the peculiar characteristics of some RGB stars (rapid rotation, magnetic fields, and lithium abundance) have been explained as the result of orbital decay and ingestion of giant planets (Carlberg et al. 2009; Aguilera-Gómez et al. 2016a, 2016b; Privitera et al. 2016a, 2016b).

The volume V over which planets of radius R_p and orbital period P can be detected transiting a star of mass M_* and radius R_* is (see the Appendix):

$$V \sim R_p^{\frac{3}{(1-\alpha)}} P^{-1} R_*^{-\frac{3(3\alpha-1)}{2(1-\alpha)}} M_*^{-\frac{1}{2}}, \tag{9}$$

where α is the power-law index relating the rms photometric error to the number of observations ($\alpha = 1/2$ for uncorrelated white noise). The lifetime of a planet against orbital decay due to tides raised on the star, in the limit that the decay time is short compared to the RGB lifetime, is

$$\tau_{\text{tide}} \approx 4.1 \left(\frac{M_P}{M_J}\right)^{-1} P_{\text{days}}^{\frac{13}{3}} \frac{Q_*'}{2 \times 10^5} \left(\frac{M_*}{M_\odot}\right)^{\frac{5}{3}} \left(\frac{R_*}{R_\odot}\right)^{-5} \text{Myr}, \quad (10)$$

where Q'_* is a modified tidal quality factor (see the Appendix). The bias effect B is the product $V \cdot \tau_{\text{tide}}$ which then scales as

$$B \propto R_p^{\frac{3}{(1-\alpha)}} M_p^{-1} P^{\frac{10}{3}} M_*^{\frac{7}{6}} R_*^{-\frac{7-\alpha}{2(1-\alpha)}}.$$
 (11)

This formulation ignores the possibility of Roche-lobe overflow and mass exchange between the planet and the star (e.g., Jackson et al. 2017 and references therein). Roche-lobe overflow of the planet will occur only when $a \lesssim 2.0R_*(\rho_*/\rho_p)^{1/3}$ (Rappaport et al. 2013), and since ρ_p is at least an order of magnitude larger than ρ_* on the RGB, overflow never occurs before the planet is engulfed. In fact, the planet may accrete mass from the star before engulfment, but this only hastens its demise.

Our survey is biased toward planets with large radii (easier to detect) but against planets with large masses (shorter lifetime). Contours of constant bias in a mass-radius diagram describe the relation $R_P \propto M_P^{(1-\alpha)/3}$. If the power-law index of the planetary mass-radius relation is steeper than the critical value $(1 - \alpha)/3$, then larger planets are favored; if it is shallower, then smaller planets are favored. A maximum in B occurs where the index breaks, i.e., at a "knee" in the mass-radius relation. For $\alpha = 1/2$, the critical value of the power-law index is 1/6, i.e., well below the values inferred for rocky planets or "ice giants" like Neptune. Chen & Kipping (2017) inferred a break at $0.41 \pm 0.06 M_J$, where the index falls from 0.59 to -0.04, reflecting the onset of support by electron degeneracy in gas giant planets. Bashi et al. (2017) found a similar transition of 0.55 to 0.01 at 0.39 \pm 0.02 M_J . Since the power-law index of B is bounded by 0 and 1/3, the location of B is independent of α , but the magnitude of the bias does increase with α . This is

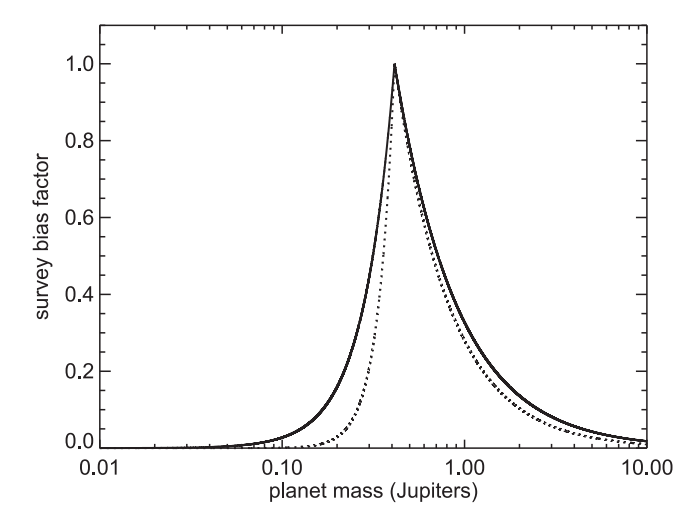


Figure 14. Survey bias factor B as a function of planet mass for planets around evolved stars, calculated using Equation (11) and the Chen & Kipping (2017) planet mass–radius relation, and assuming the orbital decay time is much shorter than the stellar evolution time. The solid line is for pure "white" (Poisson) noise ($\alpha=0.5$) while the dashed line is for the case of "red" (correlated) noise ($\alpha=0.7$). The detection of planets of $0.4M_J$ mass is strongly favored: smaller planets are more difficult to detect while more massive planets do not survive long enough.

illustrated in Figure 14, where *B* (normalized by the maximum value) is calculated for planets following the Chen & Kipping (2017) mass–radius relation and with $\alpha = 1/2$ (pure Poisson noise) and $\alpha = 0.7$ (finite correlated noise).

For periods less than a critical value P_* (see the Appendix), where

$$P_* = 0.63 (M_P \tau_{\text{RGB}} M_*^{-1} \rho_i^{-5/3})^{3/13} \text{ days},$$
 (12)

and M_P is in Jupiter masses, $\tau_{\rm RGB}$ is in Myr, and M_* and ρ_i are in solar units, the decay time is shorter than the RGB lifetime and Equation (12) holds. Using the stellar evolution models of Pols et al. (1998) for a solar-like metallicity, we find $P_* \approx 5-6$ days, roughly independent of M_* over the range 0.9–1.6 M_{\odot} , and only weakly dependent on M_P . For planets with $P > P_*$, including K2-97b and K2-132b, planet lifetime is governed by the RGB evolution time rather than orbital decay time, and detection bias dominates.

The survey bias for P can be seen in Equation (11), where B increases rapidly with P to P_* , at which point $\tau_{\rm tide}$ becomes comparable to $\tau_{\rm RGB}$ and Equation (11) no longer applies. Beyond that point, survey bias is governed by detection bias, which decreases with P (Equation (9)). Thus, B has a maximum at P=5-6 days, weakly dependent on planet mass and Q_* . This potentially can explain Kepler-91b (6.25 days), but perhaps not K2-97b or K2-132b.

Since P_* is weakly M_P dependent, the survey bias at $P=P_*$ is also dependent on both R_P and M_P . Substituting Equation (12) into Equation (11) yields $B \propto R_P^{3/(1-\alpha)} M_P^{-3/13}$. Interestingly, this mass dependence, combined with the slightly negative mass–radius power-law index for giant planets due to electron degeneracy pressure, is enough to produce a peak in B, again at the $0.4M_J$ transition. Explanation of the similarities of the K2-97b and K2-132b systems by survey bias, however, might require an anomalously low value of Q_*' , inconsistent with

constraints from binary stars and analyses of other planetary systems (see the discussion in Patra et al. 2017), as well as the theoretical expectation that dissipation on the RGB is weaker because of the small core mass and radius (e.g., Gallet et al. 2017).

Alternatively, we note that our selection criterion of detectable stellar oscillations imposes a lower limit on R_* of about $3R_{\odot}$. This means that that the effective initial stellar density in our sample ρ_i is several times smaller, which increase P_* by a factor of ~ 1.5 , making it consistent with the orbits of K2-97b and K2-132b. In a future work, we will perform a more rigorous treatment of bias using the actual stars in our survey and their properties using asteroseismology, spectroscopy, and forthcoming Gaia parallaxes.

6. Conclusions

We report the discovery of a transiting planet with $R = 1.30 \pm 0.07 R_{\rm J}$ and $M = 0.49 \pm 0.06 M_{\rm J}$ around the low-luminosity giant star K2-132, and revise our earlier mass estimate of K2-97b. We use a simple harmonic oscillator Gaussian process model to estimate the correlated noise in the light curve to quantify and remove potential correlations between planetary and stellar properties, and measure asteroseismic quantities of the star using only time domain information. We also performed spectroscopic, traditional asteroseismic, and imaging studies of the host stars K2-97 and K2-132 to precisely determine stellar parameters and evolutionary history and rule out false positive scenarios. We find that both systems have effectively null false positive probabilities. We also find that the masses, radii, and orbital periods of these systems are similar to within 10%, possibly due to a selection bias toward larger yet less massive planets.

We determine that K2-97b and K2-132b require approximately 0.03% of the current incident stellar flux to be deposited into the planets' deep convective interior to explain their radii. This suggests that planet inflation is a direct response to stellar irradiation rather than an effect of delayed planet cooling after formation, especially for inflated planets seen in evolved systems. However, stellar irradiation may not be as efficient a mechanism for planet inflation as indicated by Grunblatt et al. (2016), due to the previously overestimated mass of K2-97b driven by the limited phase coverage of the original Keck/HIRES RV measurements.

Further studies of planets around evolved stars are essential to confirm the planet re-inflation hypothesis. Planets may be inflated by methods that are more strongly dependent on other factors such as atmospheric metallicity than incident flux. An inflated planet on a 20 day orbit around a giant star would have been definitively outside the inflated planet regime when its host star was on the main sequence, and thus finding such a planet could more definitively test the re-inflation hypothesis. Similarly, a similar planet at a similar orbital period around a more evolved star will be inflated to a higher degree (assuming a constant heating efficiency for all planets). Thus, discovering such a planet would provide more conclusive evidence regarding these phenomena. Heating efficiency may also vary between planets, dependent on composition and other environmental factors. Continued research of planets orbiting subgiant stars and planet candidates around larger, more evolved stars should provide a more conclusive view of planet re-inflation.

The NASA TESS Mission (Sullivan et al. 2015) will observe over 90% of the sky with cadence and precision similar to the

K2 Mission for 30 days or more. These data will be sufficient to identify additional planets in $\sim\!10$ day orbital periods around over an order of magnitude more evolved stars, including oscillating red giants (Campante et al. 2016). This data set should be sufficient to constrain the heating efficiency of gas giant planets to the precision necessary to effectively distinguish between delayed cooling and direct re-inflationary scenarios. It will also greatly enhance our ability to estimate planet occurrence around LLRGB stars and perhaps help determine the longevity of our own planetary system.

The authors would like to thank Jonathan Fortney, Ruth Angus, Ashley Chontos, Travis Berger, Allan Simeon, Jr., Jordan Vaughan, and Stephanie Yoshida for helpful discussions. This research was supported by the NASA Origins of Solar Systems grant NNX11AC33G to E.G. and by the NASA K2 Guest Observer Award NNX16AH45G to D.H. D.H. acknowledges support by the Australian Research Council's Discovery Projects funding scheme (project number DE140101364) and support by the National Aeronautics and Space Administration under grant NNX14AB92G issued through the Kepler Participating Scientist Program. W.J.C. and T.S.H.N. acknowledge support from the UK Science and Technology Facilities Council (STFC). A.V. is supported by the NSF Graduate Research Fellowship, grant No. DGE 1144152. This research made use of the Exoplanet Orbit Database and the Exoplanet Data Explorer at exoplanets.org. This work benefited from the Exoplanet Summer Program in the Other Worlds Laboratory (OWL) at the University of California, Santa Cruz, a program funded by the Heising-Simons Foundation. This work was based on observations at the W. M. Keck Observatory granted by the University of Hawaii, the University of California, and the California Institute of Technology. We thank the observers who contributed to the measurements reported here and acknowledge the efforts of the Keck Observatory staff. We extend special thanks to those of Hawaiian ancestry on whose sacred mountain of Maunakea we are privileged to be guests. Some/ all of the data presented in this paper were obtained from the Mikulski Archive for Space Telescopes (MAST). STScI is operated by the Association of Universities for Research in Astronomy, Inc., under NASA contract NAS5-26555. Support for MAST for non-HST data is provided by the NASA Office of Space Science via grant NNX09AF08G and by other grants and contracts. This research made use of the NASA/IPAC Infrared Science Archive, which is operated by the Jet Propulsion Laboratory, California Institute of Technology, under contract with the National Aeronautics and Space Administration. This research made use of the SIMBAD and VIZIER Astronomical Databases, operated at CDS, Strasbourg, France (http://cdsweb.u-strasbg.fr/), and of NASAs Astrophysics Data System, of the Jean-Marie Mariotti Center Search service (http://www.jmmc.fr/searchcal), co-developed by FIZEAU and LAOG/IPAG. E.D.L. received funding from the European Union Seventh Framework Programme (FP7/ 2007–2013) under grant agreement number 313014 (ETAEARTH). Any opinion, findings, and conclusions or recommendations expressed in this material are those of the authors and do not necessarily reflect the views of the National Science Foundation.

Appendix

Survey Bias for Star and Planet Properties

Following Gaudi et al. (2005), we estimated the distance d to which systems can be detected, but we modify the calculation to account for coherent ("red") noise from stellar granulation and noise due to the drift of the spacecraft and stellar image on the K2 CCDs, whereby the rms noise increases faster than the square root of the number of measurements n, or the signal-tonoise ratio decreases slower than $n^{-1/2}$. We parameterize this by the index α , where the rms noise scales as n^{α} . In a magnitude-limited survey of stars of a monotonic color (i.e., bolometric correction) and fixed solid angle, the volume V that can be observed to a distance d, and hence the number of systems in a survey, goes as d^3 . This scales as²¹

$$V \propto R_p^{\frac{3}{(1-\alpha)}} P^{-1} R_*^{-\frac{3\alpha}{1-\alpha}} \rho_*^{-\frac{1}{2}}.$$
 (13)

For the case of $\alpha = 1/2$ (white noise), we recover the original scaling of Gaudi et al. (2005):

$$V \propto R_p^6 R_*^{-\frac{3}{1-\alpha}} P^{-1} \rho_*^{-\frac{1}{2}}.$$
 (14)

Since stars on the RGB differ far more in radius than they do in mass, we re-express ρ_* in Equation (9) in terms of M_* and R_* :

$$V \sim R_p^{\frac{3}{(1-\alpha)}} P^{-1} R_*^{-\frac{3(3\alpha-1)}{2(1-\alpha)}} M_*^{-\frac{1}{2}}.$$
 (15)

We also consider the lifetime of a planet against orbital decay due to the tides it raises on the slowly rotating star. This is expressed as (e.g., Patra et al. 2017)

$$\frac{dP}{dt} = -\frac{27\pi}{2Q_*'} \frac{M_P}{M_*} \left(\frac{3\pi}{G\rho_*}\right)^{\frac{5}{3}} P^{-\frac{10}{3}},\tag{16}$$

where Q'_* is a modified tidal dissipation factor that includes the Love number, M_* and ρ_* the stellar mass and mean density, and G the gravitational constant.

If a planet's orbit decays on a timescale that is short compared to any evolution of the host star on the RGB (i.e., R_* is constant) and mass loss is negligible (i.e., M_* is constant), then integrating Equation (16) yields the decay lifetime τ_{tide} :

$$\tau_{\text{tide}} \approx 4.1 \left(\frac{M_P}{M_J}\right)^{-1} P_{\text{dy}}^{\frac{13}{3}} \frac{Q_*'}{2 \times 10^5} \left(\frac{M_*}{M_\odot}\right)^{\frac{5}{3}} \left(\frac{R_*}{R_\odot}\right)^{-5} \text{Myr}, \quad (17)$$

where stellar values are those at the base of the RGB.

For sufficiently low M_P or large P, the orbital decay time becomes comparable to the timescale of evolution of the host star on the RGB. R_* increases, decreasing the volume over which the planet could be detected (Equation (9)), and shortens the lifetime (Equation (10)). Rather than $V\tau_{\rm tide}$, we must evaluate

$$B \propto \int_0^{\tau_{\rm tide}} dt \ V(t). \tag{18}$$

To model the density evolution on the RGB during H-shell burning, we adopt a helium core-mass evolution equation:

$$\frac{dM_c}{dt} = -\frac{L}{X\xi},\tag{19}$$

where L is the luminosity, X is the mixing ratio of H fuel (≈ 0.7), and ξ is the energy released during H burning. We use the coremass–luminosity relation of Refsdal & Weigert (1970),

$$\frac{L}{L_{\odot}} \approx 200 \left(\frac{M_c}{M_0}\right)^{\beta},\tag{20}$$

where $M_0 = 0.3 M_{\odot}$ is a reference core mass and $\beta = 7.6$. Assuming a constant $T_{\rm eff}$ so that $L_* \propto R_*^2$ and neglecting mass loss on the RGB, the density evolves as

$$R_* = R_i \left[1 - \frac{L_0(\beta - 1)}{M_0 X \xi} \left(\frac{M_i}{M_0} \right)^{\beta - 1} \right]^{\frac{-\beta}{2(\beta - 1)}}, \tag{21}$$

where ρ_i and M_i are the initial stellar density and core mass on the RGB. This can be rewritten in terms of the duration of the RGB phase τ_{RGB} and the final core mass M_f at the tip of the RGB when the helium flash occurs:

$$R_*(t) = R_i \left[1 + \frac{t}{\tau_{\text{RGB}}} \left[1 - \left(\frac{M_i}{M_f} \right)^{\beta - 1} \right] \right]^{\frac{-\beta}{2(\beta - 1)}}$$
 (22)

By the time the helium flash occurs, the radius of the star has evolved considerably, i.e., $R_f/R_i = (M_f/M_i)^{\beta/2}$. For a solar-mass star, $M_f/M_i \approx 4$ (Pols et al. 1998), and stars at the RGB tip will have enlarged by over two orders of magnitude relative to the end of the main sequence, while $\tau_{\rm tide}$ will have fallen by a factor of 10^{11} (Equation (10)). We assume that no planet of interest survives that long, i.e., $\tau_{\rm tide}$ never approaches $\tau_{\rm RGB}$. Moreover, even giant planets will not be detected by transit because R_P/R_* will be too small, and we neglect the mass term in Equation (22):

$$R_*(t) \approx R_i \left(1 - \frac{t}{\tau_{\text{RGR}}}\right)^{\frac{-\beta}{2(\beta-1)}}$$
 (23)

To obtain a scaling relation for τ_{tide} , we substitute Equation (22) into Equation (16), integrate to obtain P(t), then evaluate the time-dependent factors in Equation (18). Substituting $x = 1 - t/\tau_{\text{RGB}}$, B scales as

$$B \propto R_p^{\frac{3}{1-\alpha}} M_*^{-\frac{1}{2}} \tau_{\text{RGB}}$$

$$\times \int_{x_{\min}}^{1} dx \left[1 - A(x^{-\frac{3\beta+2}{2(\beta-1)}} - 1) \right]^{-\frac{3}{13}} x^{\frac{3\beta(3\alpha-1)}{4(1-\alpha)(\beta-1)}}, \quad (24)$$

where

$$A = \frac{117\pi}{Q_*} \frac{\beta - 1}{3\beta + 2} \frac{M_P}{M_*} \left(\frac{3\pi}{G\rho_i}\right)^{5/3} \frac{\tau_{\text{RGB}}}{P_0^{13/3}}$$
(25)

and

$$x_{\min} = (1 + A^{-1})^{-\frac{2(\beta - 1)}{3\beta + 2}}.$$
 (26)

Figure 15 plots B as a function of A for $\beta = 7.6$ and $\alpha = 1/2$. It shows that if $A \gg 1$ (rapid tidal evolution), then $B \propto A^{-1}$

 $[\]overline{^{21}}$ This assumes that d does not extend outside the galactic disk over a significant portion of the survey.

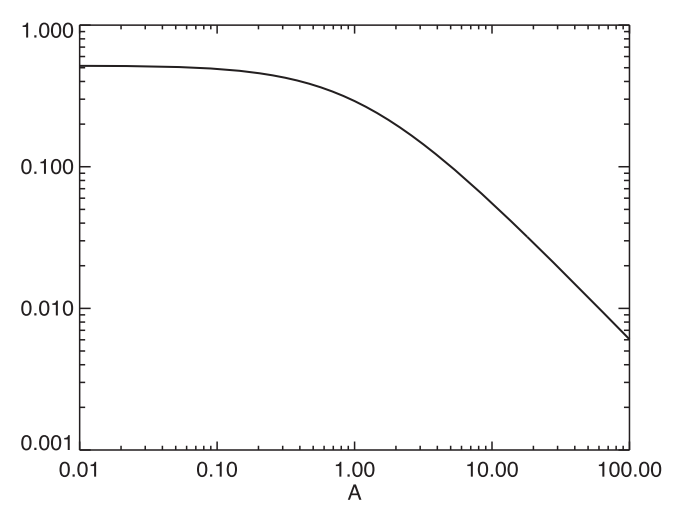


Figure 15. Survey bias factor B as a function of A (Equation (25)), which contains the dependencies on M_P , P, and R_* , and accounts for the simultaneous orbital decay and evolution of the host star along the RGB. In the regime where $A \gg 1$ (orbital decay faster than stellar evolution), $B \propto 1/A$ and Equation (11) is recovered. If $A \ll 1$, B is independent of A and depends only on R_P .

and hence $B \propto R_P^{3/(1-\alpha)} M_p^{-1}$, as in Equation (11) and thus detection of transition objects at the electron degeneracy threshold is favored. However, if $A \ll 1$, then B is independent of A, and hence M_P and P (but not R_P). Detection of gas giants, particularly inflated planets with the largest radii, is then favored. For the same values of α and β , and $Q_* = 2 \times 10^5$, the condition for A = 1 becomes a critical value for the period

$$P_* = 0.63 (M_P \tau_{\text{RGB}} M_*^{-1} \rho_i^{-5/3})^{3/13} \text{ days},$$
 (27)

where M_P is in Jupiter masses, τ_{RGB} is in Myr, and M_* and ρ_i are in solar units.

ORCID iDs

Samuel K. Grunblatt https://orcid.org/0000-0003-4976-9980

Daniel Huber https://orcid.org/0000-0001-8832-4488 Andrew W. Howard https://orcid.org/0000-0001-8638-0320

Howard T. Isaacson https://orcid.org/0000-0002-0531-1073 Evan Sinukoff https://orcid.org/0000-0002-5658-0601 Andrew Vanderburg https://orcid.org/0000-0001-7246-5438

William Chaplin https://orcid.org/0000-0002-5714-8618 Daniel Foreman-Mackey https://orcid.org/0000-0002-9328-5652

Erik Petigura https://orcid.org/0000-0003-0967-2893
Megan Ansdell https://orcid.org/0000-0003-4142-9842
Lauren Weiss https://orcid.org/0000-0002-3725-3058
Benjamin Fulton https://orcid.org/0000-0003-3504-5316
Douglas N. C. Lin https://orcid.org/0000-0001-5466-4628

References

Aguilera-Gómez, C., Chanamé, J., Pinsonneault, M. H., & Carlberg, J. K.
2016a, ApJL, 833, L24
Aguilera-Gómez, C., Chanamé, J., Pinsonneault, M. H., & Carlberg, J. K.
2016b, ApJ, 829, 127
Parentía: J. Chabrier, C. Fontony, J. & Satin, C. 2014 in Protestors and Planete.

Baraffe, I., Chabrier, G., Fortney, J., & Sotin, C. 2014, in Protostars and Planets VI, ed. H. Beuther et al. (Tucson, AZ: Univ. Arizona Press), 763

```
Barclay, T., Endl, M., Huber, D., et al. 2015, ApJ, 800, 46
Bashi, D., Helled, R., Zucker, S., & Mordasini, C. 2017, A
Batygin, K., & Stevenson, D. J. 2010, ApJL, 714, L238
Bodenheimer, P., Lin, D. N. C., & Mardling, R. A. 2001, ApJ, 548, 466
Bressan, A., Marigo, P., Girardi, L., et al. 2012, MNRAS, 427, 127
Brewer, B. J., & Stello, D. 2009, MNRAS, 395, 2226
Brown, T. M., Gilliland, R. L., Noyes, R. W., & Ramsey, L. W. 1991, ApJ,
Burrows, A., Guillot, T., Hubbard, W. B., et al. 2000, ApJL, 534, L97
Burrows, A., Marley, M., Hubbard, W. B., et al. 1997, ApJ, 491, 856
Butler, R. P., Marcy, G. W., Williams, E., et al. 1996, PASP, 108, 500
Campante, T. L., Schofield, M., Kuszlewicz, J. S., et al. 2016, ApJ, 830, 138
Carlberg, J. K., Majewski, S. R., & Arras, P. 2009, ApJ, 700, 832
Carter, J. A., & Winn, J. N. 2009, ApJ, 704, 51
Chabrier, G., & Baraffe, I. 2007, ApJL, 661, L81
Chaplin, W. J., Basu, S., Huber, D., et al. 2014, ApJS, 210, 1
Charbonneau, D., Brown, T. M., Latham, D. W., & Mayor, M. 2000, ApJL,
Chen, J., & Kipping, D. 2017, ApJ, 834, 17
Choi, J., Dotter, A., Conroy, C., et al. 2016, ApJ, 823, 102
Claret, A., & Bloemen, S. 2011, A&A, 529, A75
Coelho, P., Barbuy, B., Meléndez, J., Schiavon, R. P., & Castilho, B. V. 2005,
   A&A, 443, 735
Dawson, R. I., Johnson, J. A., Fabrycky, D. C., et al. 2014, ApJ, 791, 89
Demory, B.-O., & Seager, S. 2011, ApJS, 197, 12
Eastman, J., Gaudi, B. S., & Agol, E. 2013, PASP, 125, 83
Foreman-Mackey, D., Agol, E., Angus, R., & Ambikasaran, S. 2017,
   arXiv:1703.09710
Foreman-Mackey, D., Hogg, D. W., Lang, D., & Goodman, J. 2013, PASP,
   125, 306
Fulton, B., & Petigura, E. 2017, radvel 0.9.1, Zenodo, doi:10.5281/zenodo.
Fulton, B. J., Petigura, E. A., Howard, A. W., et al. 2017, AJ, 154, 109
Gaidos, E., Mann, A. W., & Ansdell, M. 2016, ApJ, 817, 50
Gallet, F., Bolmont, E., Mathis, S., Charbonnel, C., & Amard, L. 2017,
   arXiv:1705.10164
Gaudi, B. S., Seager, S., & Mallen-Ornelas, G. 2005, ApJ, 623, 472
Gelman, A., & Rubin, D. B. 1992, StaSc, 7, 457
Gibson, N. P., Aigrain, S., Pont, F., et al. 2012, MNRAS, 422, 753
Ginzburg, S., & Sari, R. 2016, ApJ, 819, 116
Grunblatt, S. K., Howard, A. W., & Haywood, R. D. 2015, ApJ, 808, 127
Grunblatt, S. K., Huber, D., Gaidos, E. J., et al. 2016, AJ, 152, 185
Gu, P.-G., Lin, D. N. C., & Bodenheimer, P. H. 2003, ApJ, 588, 509
Guillot, T., & Showman, A. P. 2002, A&A, 385, 156
Harvey, J. 1985, in ASP Conf. Ser. 235, ESA Future Missions in Solar,
   Heliospheric & Space Plasma Physics, ed. E. Rolfe & B. Battrick (San
   Francisco, CA: ASP), 199
Haywood, R. D., Collier Cameron, A., Queloz, D., et al. 2014, MNRAS,
Henry, G. W., Marcy, G. W., Butler, R. P., & Vogt, S. S. 2000, ApJL, 529, L41
Howell, S. B., Sobeck, C., Haas, M., et al. 2014, PASP, 126, 398
Huber, D. 2016, in IAU Focus Meeting 29 (Cambridge: Cambridge Univ.
   Press), 620
Huber, D., Bedding, T. R., Arentoft, T., et al. 2011a, ApJ, 731, 94
Huber, D., Bedding, T. R., Stello, D., et al. 2011b, ApJ, 743, 143
Huber, D., Bryson, S. T., Haas, M. R., et al. 2016, ApJS, 224, 2
Huber, D., Stello, D., Bedding, T. R., et al. 2009, CoAst, 160, 74
Jackson, B., Arras, P., Penev, K., Peacock, S., & Marchant, P. 2017, ApJ,
   835, 145
Johnson, J. A., Petigura, E. A., Fulton, B. J., et al. 2017, AJ, 154, 108
Jones, M. I., Brahm, R., Espinoza, N., et al. 2017, arXiv:1707.00779
Kallinger, T., De Ridder, J., Hekker, S., et al. 2014, A&A, 570, A41
Kjeldsen, H., & Bedding, T. R. 1995, A&A, 293, 87
Kovács, G., Zucker, S., & Mazeh, T. 2002, A&A, 391, 369
Kunitomo, M., Ikoma, M., Sato, B., Katsuta, Y., & Ida, S. 2011, ApJ, 737, 66
Laughlin, G., Crismani, M., & Adams, F. C. 2011, ApJL, 729, L7
Lopez, E. D., & Fortney, J. J. 2016, ApJ, 818, 4
Mandel, K., & Agol, E. 2002, ApJL, 580, L171
Mathur, S., Metcalfe, T. S., Woitaszek, M., et al. 2012, ApJ, 749, 152
Metchev, S. A., & Hillenbrand, L. A. 2009, ApJS, 181, 62
North, T. S. H., Campante, T. L., Miglio, A., et al. 2017, MNRAS, 472, 1866
Ogilvie, G. I., & Lin, D. N. C. 2004, ApJ, 610, 477
Patra, K. C., Winn, J. N., Holman, M. J., et al. 2017, AJ, 154, 4
Petigura, E. A. 2015, PhD thesis, Univ. California
```

Petigura, E. A., Howard, A. W., Marcy, G. W., et al. 2017, AJ, 154, 107

```
Pols, O. R., Schröder, K.-P., Hurley, J. R., Tout, C. A., & Eggleton, P. P. 1998,
MNRAS, 298, 525
```

```
Privitera, G., Meynet, G., Eggenberger, P., et al. 2016a, A&A, 593, A128
Privitera, G., Meynet, G., Eggenberger, P., et al. 2016b, A&A, 593, L15
```

Rappaport, S., Sanchis-Ojeda, R., Rogers, L. A., Levine, A., & Winn, J. N. 2013, ApJL, 773, L15

Rasmussen, C. E., & Williams, C. K. I. 2006, Gaussian Processes for Machine Learning (Cambridge, MA: MIT Press)

Refsdal, S., & Weigert, A. 1970, A&A, 6, 426

Sharma, S., Stello, D., Bland-Hawthorn, J., Huber, D., & Bedding, T. R. 2016, ApJ, 822, 15

Stello, D., Cantiello, M., Fuller, J., Garcia, R. A., & Huber, D. 2016, PASA, 33, e011

Sullivan, P. W., Winn, J. N., Berta-Thompson, Z. K., et al. 2015, ApJ, 809, 77

Thorngren, D. P., Fortney, J. J., & Lopez, E. D. 2016, ApJ, 831, 64 Tremblin, P., Chabrier, G., Mayne, N. J., et al. 2017, ApJ, 841, 30

Vanderburg, A., Latham, D. W., Buchhave, L. A., et al. 2016, ApJS, 222, 14 Vogt, S. S., Allen, S. L., Bigelow, B. C., et al. 1994, Proc. SPIE, 2198, 362 Wu, Y. 2005, ApJ, 635, 688

Wu, Y., & Lithwick, Y. 2013, ApJ, 763, 13

Yu, J., Huber, D., Bedding, T. R., et al. 2016, MNRAS, 463, 1297